Boise State University
ScholarWorks

Materials Science and Engineering Faculty Publications and Presentations

Micron School for Materials Science and Engineering

5-2022

Multiphase Layered Transition Metal Oxide Positive Electrodes for Sodium Ion Batteries

Eric Gabriel
Boise State University

Dewen Hou
Boise State University

Eungjie Lee
Argonne National Laboratory

Hui Xiong
Boise State University

Received: 15 November 2021 | Revised: 8 February 2022 | Accepted: 11 February 2022

DOI: 10.1002/ese3.1128

REVIEW

Multiphase layered transition metal oxide positive electrodes for sodium ion batteries

Eric Gabriel[1] | Dewen Hou[1] | Eungje Lee[2] | Hui Xiong[1]

[1]Micron School of Materials Science and Engineering, Boise State University, Boise, Idaho, USA

[2]Argonne National Laboratory, Chemical Sciences and Engineering Division, Lemont, Illinois, USA

Correspondence
Hui Xiong, Micron School of Materials Science and Engineering, Boise State University, Boise, ID 83725, USA.
Email: clairexiong@boisestate.edu

Funding information
U.S. Department of Energy, Grant/Award Number: DE-SC0019121

Abstract

Multiphase layered transition metal oxides (LTMOs) for sodium ion battery (SIB) positive electrodes with phase interfaces across multiple length scales are a promising avenue toward practical, high-performance SIBs. Combinations of phases can complement each other's strengths and mitigate their weaknesses if their interfaces are carefully controlled. Intra- and interparticle phase interactions from nanoscale to macroscale must be carefully tuned to generate distinct effects on properties and performance. An informed design strategy must be paired with relevant synthesis techniques and complemented by spatially resolved characterization tools to manipulate different length scales and interfaces. This review examines the design, synthesis, and characterization strategies that have been demonstrated for the preparation of heterogeneous, multiphasic LTMOs with phase interfaces across varied length scales.

KEYWORDS

heterogeneous materials, layered transition metal oxides, multiphase materials, positive electrodes, sodium ion batteries

1 | INTRODUCTION

Sodium ion batteries (SIBs) have generated a great deal of interest over the last decade, with the number of publications per year on the subject increasing in excess of 1000% over the 2010–2020 time period.[1] This area of interest is driven by the rapidly increasing demand for lithium resources, which is caused primarily by the growth of the electric vehicle market.[1] The price of lithium ion battery (LIB) materials is increasing as a result of this demand (500% increase in price of Li_2CO_3 from 2000 to 2019),[2] which motivates the exploration of alternative technologies for energy storage that use cheaper and more abundant elements. Other than rising prices, the stability of the raw materials (e.g., nickel, cobalt) supply chain is another major concern for LIB applications.[3] SIBs are one attractive alternative due to the abundance of sodium, which is 23,600 ppm in Earth's crust compared to only 20 ppm for Li.[4] The electrochemical activity of sodium with iron[5] (56,000 ppm)[4] and all other 3d transition metals is an advantage compared to lithium,[6] which is only active and reversible with a select few elements (Ni, Co, Mn, Ti).[7] The comparable potential of Na/Na^+ redox ($E^0 = -2.71$ V vs. standard hydrogen electrode compared to -3.04 V for Li/Li^+),[8] sodium's nonreactivity with aluminum that allows expensive Cu current collectors (used in LIBs) to be replaced by cheap Al,[8,9] and the higher mobility of Na^+ compared to Li^+ in organic solvent such as propylene carbonate make it an excellent prospect for large-scale energy storage.[8]

This is an open access article under the terms of the Creative Commons Attribution License, which permits use, distribution and reproduction in any medium, provided the original work is properly cited.
© 2022 The Authors. *Energy Science & Engineering* published by Society of Chemical Industry and John Wiley & Sons Ltd.

The more extensively researched Li-based positive electrodes show significant similarity with Na-based positive electrodes,[10] but the larger size of Na^+ compared to Li^+ and their different electronegativities result in important differences in structure, charge storage, and transport mechanisms. In particular, the stability of SIBs over many charge/discharge cycles is poor in comparison to LIBs. The structural and electrochemical instability in Na-based positive electrode materials is one major factor that leads to the SIB performance degradation. As SIBs grow closer to large-scale commercialization (as suggested by increasing number of full cell studies),[1] a complete understanding of the mechanisms that drive instability of Na-based positive electrode materials is critical to address the increasing need for low-cost energy storage systems. The class of insertion-type electrode materials based on layered transition metal oxides (LTMOs) have received great attention. Numerous single phase LTMO positive electrode materials have been synthesized and their degradation mechanisms carefully studied.[6,11–16] A growing area of research for SIB positive electrodes is multiphase LTMO materials, which can possibly capture the benefits of a combination of single-phase materials but with less susceptibility to the degradation pathways observed in single-phase materials. Methods for the design, synthesis, and characterization of multiphase LTMOs as positive electrode materials are important to develop further understanding of high-performance SIB positive electrode materials (Figure 1). The purpose of this review is to provide examples that help answer the following questions:

1. What types of heterogeneity and phase interfaces exist in multiphase LTMOs?
2. What are the benefits of multiphase LTMOs to electrochemical properties?
3. How can multiphase LTMO materials be designed, characterized, and synthesized?

1.1 | Single phase layered transition metal oxides (LTMOs)

Sodium based LTMOs with composition Na_xTMO_2 (TM = transition metal, e.g., Ni, Fe, Mn, Co, $0.0 \leq x \leq 1.0$) are attractive positive electrode materials for SIBs due to their combination of high voltage, high theoretical capacity, and dense structure. Compared to lithium based LTMOs, sodium is electrochemically active with more of the 3d transition metal elements. The larger size of Na enables structures that are unstable in Li-based LTMO materials. The versatile combination of elements and structures in sodium based LTMOs provides many routes to tune their properties.

1.2 | Crystal structure of LTMOs

LTMOs are comprised of layers of edge sharing TMO_2 octahedra separated by layers of sodium which may have multiple site geometries. LTMOs are usually described according to the notation proposed by Delmas.[17] The Delmas notation is comprised of letter(s) (O, P, OP) describing the geometry of the sodium sites and a number (1, 2, 3, 4, 6) which describes the number of TMO_2 layers required to achieve translational symmetry along the layer stacking direction (c). Octahedral and prismatic sodium site geometries correspond to O and P, respectively. This is illustrated in Figure 2. Two of the most commonly observed structures for LTMOs are O3 (e.g., $NaFeO_2$), which has three unique TMO_2 layers with octahedral sodium site geometry and P2 (e.g., $Na_{2/3}CoO_2$), which has two unique TMO_2 layers with trigonal prismatic sodium site geometry. Commonly, O-type phases form when the sodium to transition metal ratio is near 1. P-type phases form often when this ratio is between ½ and 2/3.

The sodium site geometry is dictated by the oxygen stacking sequence. When considering stacking of

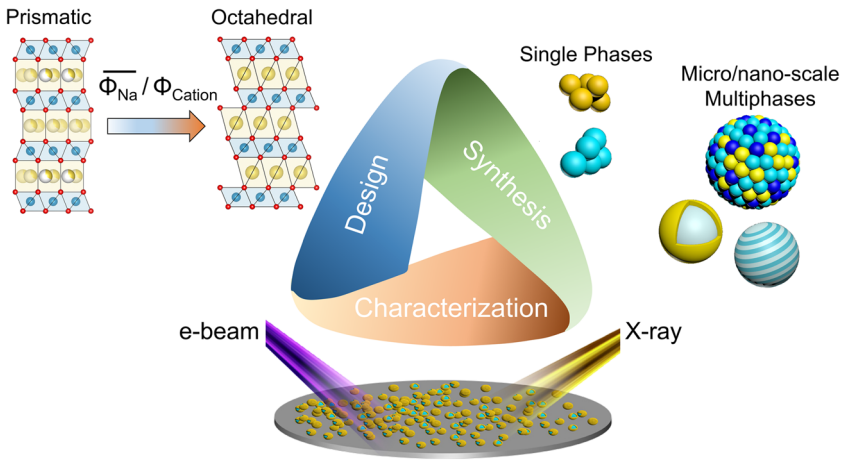

FIGURE 1 Schematic representation of the topics covered by this review—design, synthesis, and characterization of layered transition metal oxides across length scales

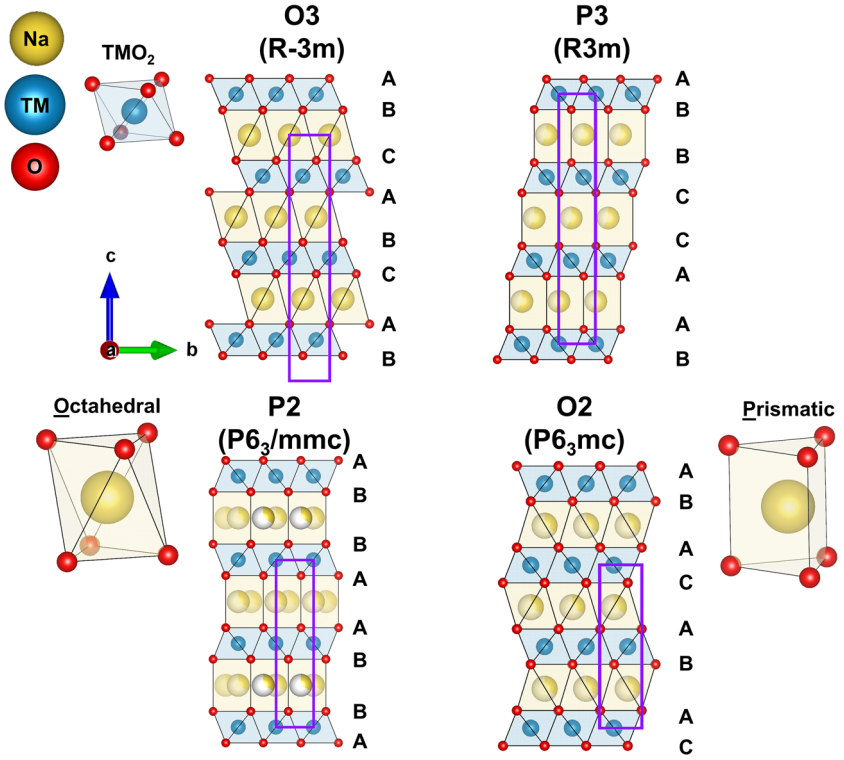

FIGURE 2 Illustration of the various LTMO structures and sodium site geometries. The purple lines indicate the edges of the unit cell. LTMO, layered transition metal oxide.

hexagonal close-packed layers, three unique layer positions are possible: A at (0, 0, z), B at (2/3, 1/3, z), and C (1/3, 2/3, z). When adjacent TMO_2 layers have different oxygen positions (e.g., AB layer adjacent CA) an octahedral sodium site geometry is formed. When the adjacent layers have the same oxygen position (e.g., AB layer adjacent BA), a prismatic sodium site geometry occurs. Structures with symmetry breaking distortions (e.g., O3-like $NaNiO_2$ with monoclinic distortion[18]) are often denoted by a prime, such as O′3 or P′3. The various structures are readily distinguished by their unique X-ray diffraction (XRD), neutron diffraction, and/or electron diffraction patterns.

1.3 | Driving forces for O- and P-type stacking

Zhao et al.[19] have shown that the tendency toward O3 or P2 type stacking can be predicted with good accuracy for single phase, thermodynamically stable materials based on the "cationic potential" (Φ_{cation}) which is a function of the transition metal and alkali elements, their oxidation states, stoichiometric ratios, and ionic radii. The mathematical construction of the cationic potential is

$$\Phi_{\text{cation}} = \frac{\overline{\Phi_{\text{TM}}} \quad \overline{\Phi_{\text{Na}}}}{\overline{\Phi_{\text{O}}}}, \tag{1}$$

$$\overline{\Phi_{\text{TM}}} = \sum \frac{w_i n_i}{R_i}, \tag{2}$$

$$\overline{\Phi_{\text{Na}}} = \frac{w_{\text{Na}}}{R_{Na}}. \tag{3}$$

$\overline{\Phi_{\text{TM}}}$ and $\overline{\Phi_{\text{Na}}}$ represent the ionic potential associated with the TMs and Na, respectively. w_i, n_i, and R_i correspond to the stoichiometric coefficient, charge, and ionic radius of species i. $\overline{\Phi_{\text{O}}}$ can be considered as constant at 28.571 nm^{-1} ($4/R_{O_2^-}$). Using a fit to over 100 experimentally obtained O3 and P2 type LTMOs, Zhao et al. showed empirically that when $\overline{\Phi_{\text{Na}}} > 0.4065\,\Phi_{\text{cation}} + 1.572\,\text{nm}^{-1}$, the O3 phase is favored (Figure 3).[19] When this inequality is reversed, the P2 phase is favored. Therefore, a high ratio of $\overline{\phi_{\text{Na}}}/\phi_{Cation}$ promotes O3 phase formation, and a low ratio favors P2 formation. A higher value of $\overline{\Phi_{\text{Na}}}$ indicates a greater ability of Na ions to screen the electrostatic repulsion between adjacent TM layers. The choice of transition metal elements and their preferred oxidation states dictates $\overline{\Phi_{\text{TM}}}$. High oxidation state ($n_i$) and small radius ($R_i$) increase $\overline{\Phi_{\text{TM}}}$, which increases the favorability of the P2 phase for fixed $\overline{\Phi_{\text{Na}}}$. A larger value of $\overline{\Phi_{\text{TM}}}$ indicates stronger localization of electrons within individual TM layers, which increases the repulsion between adjacent TM layers. This repulsion facilitates the P2 stacking when sufficiently strong. The P3 structure is not predicted by this model, but in several cases can be synthesized with identical compositions to P2 type materials, but with lower calcination temperature.[20,21]

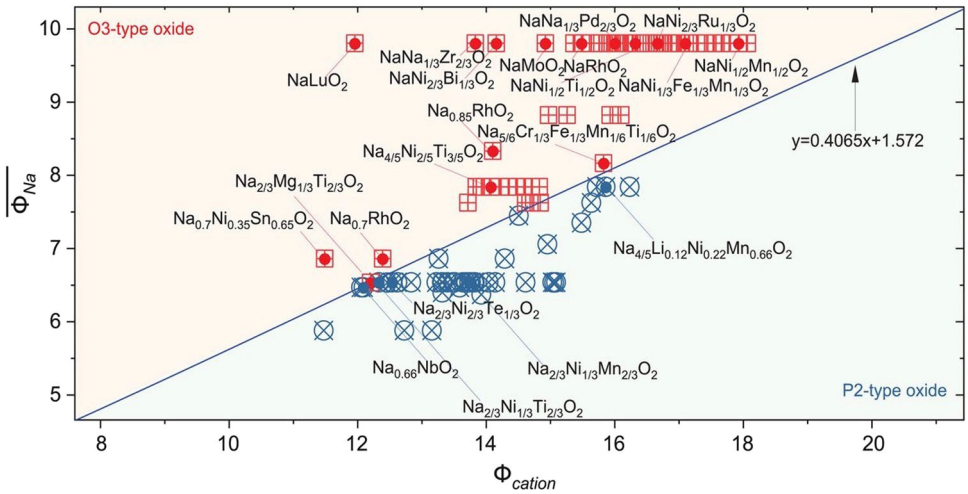

FIGURE 3 Various sodium based LTMOs with the O3 and P2 structures, which show clear tendency toward each structure depending on the sodium ionic potential and the overall cationic potential. Reprinted from Reference [19] with permission from AAAS. LTMO, layered transition metal oxide

The P3 sodium sites all share one face above or below with a TM octahedron and a vacant tetrahedral site in the TM layer on the opposite face (TM-Na-Vacancy). In contrast, the P2 sodium sites are either face-sharing with two TM octahedra (TM-Na-TM) on either side, or two tetrahedral vacancies on either side (Vacancy-Na-Vacancy). Thus, the temperature has some effect on the relative energies of the different Na site coordination. The cationic potential model also accurately captures the tendency of lithium-based LTMOs to form 3O3-type structures, and for potassium-based LTMOs to form P2-type structures.[19]

The cationic potential construction is limited in its ability to predict the development of nonequilibrium phases, distorted phases (e.g., Jahn–Teller distorted Mn^{3+} based O′3 $NaMnO_2$),[22] and metastable phases,[19,23] which have been shown to depend greatly on the synthesis conditions, especially temperature and the precursors used.[24] Intermediate phase(s) do not have to have identical composition to the overall sample.[24] The favored intermediate structure is dictated by the composition with the most negative reaction free energy, which depends on both the precursors and temperature.[24] To design positive electrode materials with a particular desired phase (or phases), one must consider both the thermodynamic and kinetic processes that influence the phase evolution during calcination.

1.4 | Structural evolution of LTMOs during charge/discharge cycles

In the process of charging to higher voltage (vs. Na/Na^+), sodium ions are removed from the structure. Due to the large size of the Na^+ ion, removal of sodium may cause phase transitions associated with the gliding of TMO_2 layers (translations of (1/3, 2/3, 0) relative to adjacent layers) and diffusion of remaining Na^+ ions to minimize the electrostatic repulsion between TMO_2 layers.[25,26] The layer gliding alters the oxygen stacking sequence between adjacent TMO_2 layers, which may modify the sodium site geometry from octahedral to prismatic (e.g., AB CA → AB BC). In the O3 and P3 type structures, all TMO_2 octahedra are oriented in the same direction (e.g., AB, BC, CA). When distinct TMO_2 orientations coexist (AB/BC/CA vs. BA/CB/AC) as in the O2 and P2 structures, electrochemically induced phase transitions associated with each phase are limited to those that do not require the breaking of TM-oxygen bonds. Thus, O3 may glide to P3 but not P2 or O2. Similarly, P2 may glide to O2 but not O3 or P3.

These phase transitions are often partially or completely irreversible and may cause significant strain on the crystal structure, leading to poor reversibility of the electrochemical desodiation/sodiation processes. Compared to their lithium-ion counterparts, the sodium based LTMOs suffer from accelerated capacity decay due to phase transition as a result of the larger size of the Na^+ ion (102 pm) compared to the Li^+ ion (76 pm). The study of methods to mitigate the detrimental phase transitions which occur during charge and discharge is of great importance for the development of practical SIBs.

2 | MULTIPHASE LTMOS

Single-phase LTMOs with the O3 and P2 structures with a wide range of transition metal compositions (unary and multicomponent) have been studied extensively for application as positive electrode materials for SIBs.[12] Many of these materials show promising performance, but still fall short in

one or more categories (capacity, stability, power). O3-type materials have high theoretical capacities associated with their generally higher Na content but may suffer from severe capacity fading over many cycles and demonstrate underwhelming power density.[5,27–32] The higher charge cutoff voltages (>4 V vs. Na/Na^+) required to extract most Na^+ from O3-type positive electrodes are associated with a number of degradation mechanisms severely impacting the reversibility. Electrochemically induced irreversible phase transitions, oxygen release, reaction with electrolyte, and transition metal migration to the sodium layer adversely affect the performance of the electrode. Consequently, the practical capacity of O3-type positive electrodes is often significantly less than the theoretical capacity because the voltage range must be limited.[33–36] In contrast to O3-type materials, P-type materials often demonstrate excellent power performance but can be limited by their low theoretical capacity and suffer from similar degradation mechanisms as O3-type materials.[37–48] Other than electrochemical degradation, a significant barrier to the practical application of LTMOs is their vulnerability to degradation resulting from exposure to air.[49,50] Exposure to water and carbon dioxide in air can cause extraction of sodium from the structure and/or intercalation of water or carbonate ions, while forming residues of sodium hydroxide or sodium carbonate.[51–54] These residues may have multiple negative effects, including reduced capacity, Coulombic efficiency, and/or reaction with the binder.[49,52] Protecting LTMO materials from air can circumvent this issue, but introduces undesirable cost and complexity of processing, which is especially problematic for industrialization. Extensive effort has been made to address the chemical and electrochemical degradation mechanisms affecting single-phase O3 and P2 materials. Common strategies for enhancing the performance and stability of single-phase materials include cationic substitution[10,55–63] and optimized electrolyte formulations.[64–66] Meanwhile, attempting to balance the benefits and drawbacks of the O- and P- type structures, a number of multiphase materials with combinations of both O- and P- type phases have demonstrated enhanced electrochemical performance compared to single-phase materials.

2.1 | Phase interactions across length scales—From macroscopic mixtures to atomic intergrowth

The simple mixture of two or more noninteracting phases would result in an electrode with intermediate, but similar properties weighted by the fraction of each phase. However, there is significant evidence that multiphase LTMOs can provide superior performance than what would be expected from a simple mixture, which suggests that interaction between the different phases is an important factor toward the electrochemical performance. To interpret the nature of the multiphase interaction, it is important to consider the length scale at which the interaction takes place. In a simple mixture (a blend of separately prepared single-phase materials), one could imagine that at the length scale of the entire electrode (millimeter and larger) there could be mechanical, electronic, ionic, and chemical interactions between phases indirectly through the matrix (binder and conducting agents) or electrolyte (Figure 4). Silicon/graphite composite anodes for LIBs are a prime example of such electrode-scale interactions, where the large volume expansion and poor conductivity of silicon must be mitigated by careful control over the spatial arrangement of graphite, silicon, and other components to prevent cracking and loss of contact with electrolyte and electronically conducting additives.[67,68] Even the morphology of the current collector, which could be thought of as a distinct but separate electrochemically inactive phase, can have significant interaction with the active materials and affect performance.[69] LTMOs as positive electrodes in SIBs have significantly less volume change compared to alloy-type electrode materials such as silicon, so electrode-scale effects are likely to be of secondary importance compared to interactions between phases at smaller length scales.

At the microscale (between 100 nm and 100 μm), when multiple phases are combined within secondary particles (large agglomerates of primary particles) the interaction between the phases should be more direct. Fast ion and/or electron conducting phases (e.g., P2) when in close contact with slow-conducting phases (e.g., O3) could facilitate faster the transport of sodium from the surface of a particle into the bulk compared to a pure slow-conducting phase. Materials that are stable against electrolyte decomposition and air could physically encapsulate more reactive

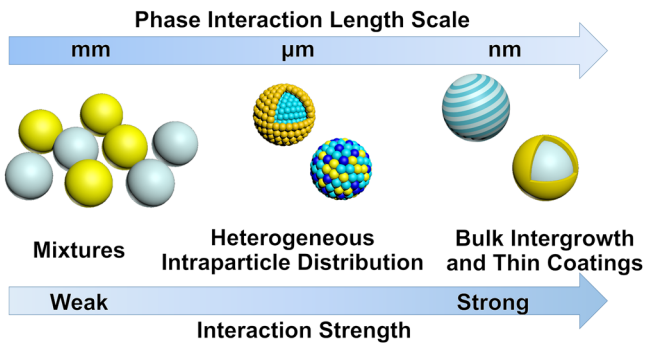

FIGURE 4 The spatial distribution of phases in multiphase LTMOs modifies the interaction strength and mechanism. LTMO, layered transition metal oxide

materials but still allow Na transport, enhancing safety and electrochemical stability. This strategy (Figure 4) has been effectively demonstrated in LIB and SIB materials, where many examples of coatings or core-shell type structures result in significantly enhanced electrochemical properties. Depending on the thickness of the coating/shell material, there may be significant differences in the mechanism of performance enhancement. Thin coatings (<100 nm) of materials such as Al_2O_3, MgO, and spinel-like Ti(III)-oxide can influence the surface reactivity with the electrolyte, air sensitivity, and electronic/ionic conductivity at the surface but they do not necessarily participate in charge compensation during cycling.[22,70–74] In contrast, thick, electrochemically active shell coating(s) around a core of different composition/phase can delay phase transition and reduce lattice expansion during charge in addition to protecting the core from reaction with electrolyte.[75,76] The possible benefit of techniques which modify the interface of the secondary particles is evident, but phase interfaces at even smaller scale within the bulk of primary particles can still provide further benefit.

Atomically integrated multiphase LTMOs have been directly observed in both sodium and lithium positive electrode materials.[77–84] Nanometer-scale domains of different phases can become integrated along the layer stacking direction (*c*-axis), which could be expected due to the close match of the in-plane interatomic distances (i.e., *a* lattice parameter in O3/P3/P2). Phase intergrowth in this manner will result in strong interactions between each phase (Figure 4). Slight mismatches between the lattice parameters at the phase boundary would result in microstrain that could affect the electrochemical properties. Consider intergrown O3 and P2 phases undergoing the electrochemical charging process. If a potential is reached where sodium would normally be extracted from the O3 phase, but a higher potential is needed to desodiate the P2 phase, a strain would result from the in-plane shrinkage (due to TM oxidation) experienced by the desodiated O3 phase while the in-plane P2 distances are unchanged. Layer gliding transitions (e.g., P2 → O2) could be pinned near the phase interface as a result of this strain. The chemo-mechanical coupling between intergrown phases has been suggested as a possible mechanism for the enhanced stability that intergrown multiphase electrode materials sometimes display.[84] The intergrowth interface between P2 and O3 type phases may also benefit the rate performance compared to pure O3 phase.[79] A higher degree of intergrowth, that is, a smaller domain size between phase interfaces, could possibly result in different effects on the electrochemical properties compared to larger coherent phase domains. Multiphase intergrowth is an area that warrants significant additional investigation and fundamental understanding, but the synthesis and characterization of intergrown multiphase materials is highly challenging.

Strategies for the synthesis of multiphase positive electrode materials should be utilized with the desired phase interface (surface or bulk) and length scale (μm–nm) in mind. Interactions at the electrode-level, particle-level, and within single crystallites can all significantly affect the electrochemical performance in unique and synergistic ways. The properties of select multiphase materials are summarized in Table 1.

3 | SYNTHESIS, PROPERTIES, AND CHARACTERIZATION OF MULTIPHASE LTMOs

3.1 | Synthesis principles

Many synthetic methods exist to prepare LTMOs for use as positive electrodes for SIBs such as solid state reaction,[101] spray pyrolysis,[102,103] and ion exchange.[104] However, by far the most common is via solid state reactions between transition metal precursor compound(s) (e.g., $Ni_{0.5}Mn_{0.5}(OH)_2$ or Fe_2O_3) and a source of sodium (e.g., Na_2CO_3, Na_2O, or NaOH) and any dopant compounds. The first critical step is the selection of the transition metal precursor compound. In unary systems (e.g., $NaFeO_2$) the oxides of the transition metal (Fe_2O_3 or Fe_3O_4) can simply be used as purchased. However, in multicomponent systems precursor compounds may not be commercially available with the desired stoichiometry. While a combination of various transition metal oxides can be used, this process may lead to poor transition metal uniformity and limited morphology control, resulting in phase separation or impurity formation during calcination as it relies on diffusion for the mixing of transition metal elements.[101] The LTMO structure is highly sensitive to the transition metal composition because it dictates the cationic potential. Consequently, both the homogeneity and purity of the transition metal precursor compound are critical to synthesize the designed material. The preparation of transition metal precursor compounds with high purity and transition metal uniformity is most commonly done by coprecipitation or sol-gel method.[101]

The precursor is combined stoichiometrically with a sodium source (e.g., sodium carbonate) and formed into a pellet, then calcined at high temperature (typically, 700–1000°C for 8–48 h) to produce the positive electrode material of interest according to a reaction similar to

$$\mathrm{TM(OH)_2} + x\mathrm{Na_2CO_3} \xrightarrow{T=700-1000^\circ\mathrm{C}} \mathrm{Na_{2x}TMO_2} + \mathrm{H_2O}\uparrow + \mathrm{CO_2}\uparrow . \quad (4)$$

TABLE 1 Summary of electrochemical properties of select multiphase LTMO positive electrode materials for SIBs

Material	Phases	Phase interface	Discharge capacity (mAh/g)	Voltage range (V, vs. Na/Na^+)	Capacity retention	Comment	References
$Na_{0.8}[(Ni_{0.5}Co_{0.2}Mn_{0.3})_{0.6}(Ni_{0.33}Mn_{0.67})_{0.4}]O_2$	O3-O′3/P2	Microscale core-shell, nanoscale P2/O3 interface in bulk	146 at 15 mA/g	1.5–4.0	75% at 200 Cycles at 75 mA/g		[75]
$Na_{0.9}Cu_{0.2}Fe_{0.28}Mn_{0.52}O_2$	O3+P3	Microscale mixture in bulk and surface	125 at 10 mA/g	2.0–4.0	99.3% at 100 Cycles at 10 mA/g		[85]
$Na_{0.65}Mn_{0.70}Ni_{0.16}Co_{0.14}O_2$@$NaTi_2(PO_4)_3$	P2@NASICON	Nanoscale surface coating	206.7 at 24 mA/g	1.5–4.3	88.3% at 100 Cycles at 240 mA/g	3 wt% coating, liquid coating process 83 mA/g at 2400 mA/g	[86]
Na2/3[Ni1/3Mn2/3]O2@NaCaPO4	P2@β-$NaCaPO_4$	Nanoscale surface coating	~150 at 20 mA/g	2.5–4.3	74% at 200 Cycles at 40 mA/g	0.5 wt% coating, liquid coating process	[87]
$Na_{2/3}[Ni_{1/3}Mn_{2/3}]O_2$@$Mg_{(1-x)}Ni_xO$	P2@Rocksalt	Nanoscale surface coating	140.6 at 8.65 mA/g	2.0–4.5	71.3% at 200 cycles at 86.5 mA/g	2 wt% coating, liquid coating process good cycling stability at 60°C	[88]
$Na_{0.7}MnO_{2.05}$@$AlPO_4$	P2@$AlPO_4$	Nanoscale surface coating	154.3 at 20 mA/g	2.0–-4.5	92.4% at 100 Cycles at 1000 mA/g	5 wt% coating, liquid coating process	[89]
$Na_{0.7}MnO_{2.05}$@$NaPO_3$	P2@$NaPO_3$	Nanoscale surface coating	162 at 100 mA/g	1.8–4.3	82% at 200 Cycles at 100 mA/g	95.5 mAh/g at 3000 mA/g, liquid coating process	[90]
$NaMn_{0.8}Ti_{0.1}Ni_{0.1}O_2$	P2@O′3@Spinel	Multiscale: Nanoscale spinel coating on O′3, microscale P2@O′3 with nanoscale P2/O′3 interfaces in bulk	186 at 20 mA/g	1.5–4.2	86% at 100 Cycles at 200 mA/g	Air stable, coating forms spontaneously 576 Wh/kg at 20 mA/g.118 mAh/g at 1000 mA/g	[22]
$Na_{0.66}Ni_{0.26}Zn_{0.07}Mn_{0.67}O_2$@ZnO	P2@Wurtzite	Nanoscale surface coating	122.4 at 10 mA/g	2.0–4.3	83.7% at 100 Cycles at 100 mA/g	Air stable, coating forms spontaneously	[91]
$Na_{0.67}Mn_{0.7}Fe_{0.2}Co_{0.1}O_2$@$ZrO_2$	P2@ZrO_2	Nanoscale surface coating	171 at 10 mA/g	1.5–4.2	89% at 10 mA/g	Coating forms spontaneously	[92]

TABLE 1 (Continued)

Material	Phases	Phase interface	Discharge capacity (mAh/g)	Voltage range (V, vs. Na/Na^+)	Capacity retention	Comment	References
$Na_{2/3}Ni_{1/3}Mn_{2/3}O_{2@Al2O3}$	P2@Al2O_3	Nanoscale surface coating	142.6 at C/20	2.3–4.5	54.3% at 100 Cycles at C/20	Atomic layer deposition coating (1 nm) on electrode	[72]
$Na_{0.66}Mn_{0.9}Mg_{0.1}O_2$@Alucone	P2@Alucone	Nanoscale surface coating	163.1 at 200 mA/g	2.0–4.5	86% at 100 Cycles at 200 mA/g	Molecular layer deposition coating (5 cycles) on electrode	[93]
$NaNi_{0.5}Mn_{0.5}O_2$@Al_2O_3	O3@Al_2O_3	Nanoscale surface coating	~108 mAh/g at 120 mA/g	2.0–4.0	68% at 300 Cycles at 120 mA/g	Atomic layer deposition coating (20 cycles) on electrode.	[94]
$Na_{2/3}(Mn_{0.54}Ni_{0.13}Co_{0.13})O_2$@$Al_2O_3$	P2@Al_2O_3	Nanoscale surface coating	123 at 160 mA/g	2.0–4.5	~63% at 100 Cycles at 160 mA/g	Atomic layer deposition coating (2 cycles) on electrode.	[95]
$Na_{0.88}Ni_{0.45}Mn_{0.55}O_2$	O3/P2 (88.4%/11.6%)	Nanoscale intergrowth in bulk	127.7 at 7.5 mA/g	2.0–4.0	71.1% at 250 Cycles at 150 mA/g		[96]
$Na_{0.85}Mn_{0.5}Ni_{0.4}M_{0.1}O_2$ (M = Ti, Fe, Cu, and Mn,)	O3/P2	Nanoscale intergrowth in bulk		2.0–4.0		>60% of 12 mA/g capacity retained at 1200 mA/g	[96]
M = Ti	O3 (100%)	Single phase	131 at 12 mA/g	2.0–4.0	91% at 500 Cycles at 120 mA/g	Air stable	[96]
M = Fe	O3/P2 (87.7%/12.3%)	Nanoscale intergrowth in bulk	130 at 12 mA/g	2.0–4.0	86.2% at 500 Cycles at 120 mA/g	Air stable	[96]
M = Cu	O3/P2 (62.1%/37.9%)	Nanoscale intergrowth in bulk	117 at 12 mA/g	2.0–4.0	90.6% at 500 Cycles at 120 mA/g	Air stable	[96]
M = Mn	O3/P2 (86.7%/13.3%)	Nanoscale intergrowth in bulk	~112 at 12 mA/g	2.0–4.0	81.5% at 500 Cycles at 120 mA/g		[96]

(Continues)

TABLE 1 (Continued)

Material	Phases	Phase interface	Discharge capacity (mAh/g)	Voltage range (V, vs. Na/Na^+)	Capacity retention	Comment	References
$Na_{0.78}Ni_{0.2}Fe_{0.38}Mn_{0.42}O_2$	O3/P2 (68.3%/31.7%)	Nanoscale intergrowth in bulk	86 at C/10	2.5–4.0	92% at 100 Cycles at C/10		[81]
$Na_{0.67}Mn_{0.64}Co_{0.30}Al_{0.06}O_2$	P2/P3 (62.2%/37.8%)	Nanoscale intergrowth in bulk	160 at 20 mA/g	1.5–4.0	73% at 100 Cycles at 200 mA/g	83 mAh/g at 1700 mA/g	[97]
$Na_{0.78}Cu_{0.26}Zn_{0.07}Mn_{0.67}O_2$	P2/P3 (95.5%/4.5%)	Nanoscale intergrowth in bulk	84 at 100 mA/g	2.5–4.1	85% at 200 Cycles at 100 mA/g	Hydrostable	[98]
$Na_{0.7}Li_{0.3}Ni_{0.5}Mn_{0.5}O_2$	O3/O′3/P3/P2	Nanoscale intergrowth in bulk	~125 at 15 mA/g	2.0–4.05	No long-term cycling	~119 mA/g at 150 mA/g	[79]
$Li_{0.25}Na_{0.87}Ni_{0.4}Fe_{0.2}Mn_{0.4}O_{2+\delta}$	O3/spinel (94%/6%)	Nanoscale intergrowth in bulk	131 at 12 mA/g	2.0–4.2 V	86% at 100 Cycles at 100 mA/g	112 mA/g at 100 mA/g	[58]
$Na_{0.67}Ni_{0.33}Mn_{0.57}Sn_{0.1}O_2$	O3/P2 (50.9%/49.1%)	Nanoscale intergrowth in bulk	155.2 at 15 mA/g	2.0–4.3	No long-term cycling		[99]
$Na_{0.62}Ni_{0.33}Mn_{0.62}Sb_{0.05}O_2$	P2/O3 (69%/31%)	Nanoscale intergrowth in bulk	105.6 at 20 mA/g	2.0–4.2	71.3% at 200 Cycles at 500 mA/g		[100]
$NaNi_{1/3}Mn_{1/3}Co_{1/3}O_2$	P2/O1/O3 (42.7%/ 39.5%/17.8%)	Nanoscale intergrowth in bulk	142.8 at 15 mA/g	2.0–4.4	80% at 100 Cycles at 75 mA/g		[84]
$Na_{0.62}Li_{0.18}Mn0_{.66}Ni_{0.17}Co_{0.17}O_2$	P3/P2/Li-O′3 (77.5%/15.5%/8%)	Nanoscale intergrowth in bulk	224 at 20 mA/g	1.5–4.5	78% at 50 Cycles at 40 mA/g		[83]
$Na_{0.66}Li_{0.18}Mn_{0.71}Ni_{0.21}Co_{0.08}O_{2+\delta}$	P2/O3 (94.2%/5.8%)	Nanoscale intergrowth in bulk	200 at 10 mA/g	1.5–4.5	75% at 150 Cycles at 50 mA/g	640 Wh/kg	[80]

3.2 | Microscale phase interfaces

Microscale phase interfaces, such as those within secondary particles, can synergistically enhance the electrochemical properties and mitigate degradation without directly modifying the properties of the individual phases. When compared to coprecipitation, the sol-gel method provides minimal control over secondary particle morphology and favors homogeneous transition metal distribution. For the synthesis of compositionally heterogeneous (e.g., core-shell or concentration gradient) electrode materials, coprecipitation can be a powerful technique to control compositional distribution between the core and surface of secondary particles.

3.2.1 | Spatial manipulation of ionic potential

Chen and coworkers utilized the coprecipitation method to prepare a O3-O′3/P2 composite electrode, designed to have core-shell composition $Na_{0.8}[(Ni_{0.5}Co_{0.2}Mn_{0.3})_{0.6}(Ni_{0.33}Mn_{0.67})_{0.4}]O_2$ through the preparation of a compositionally heterogeneous precursor (Figure 5).[75]

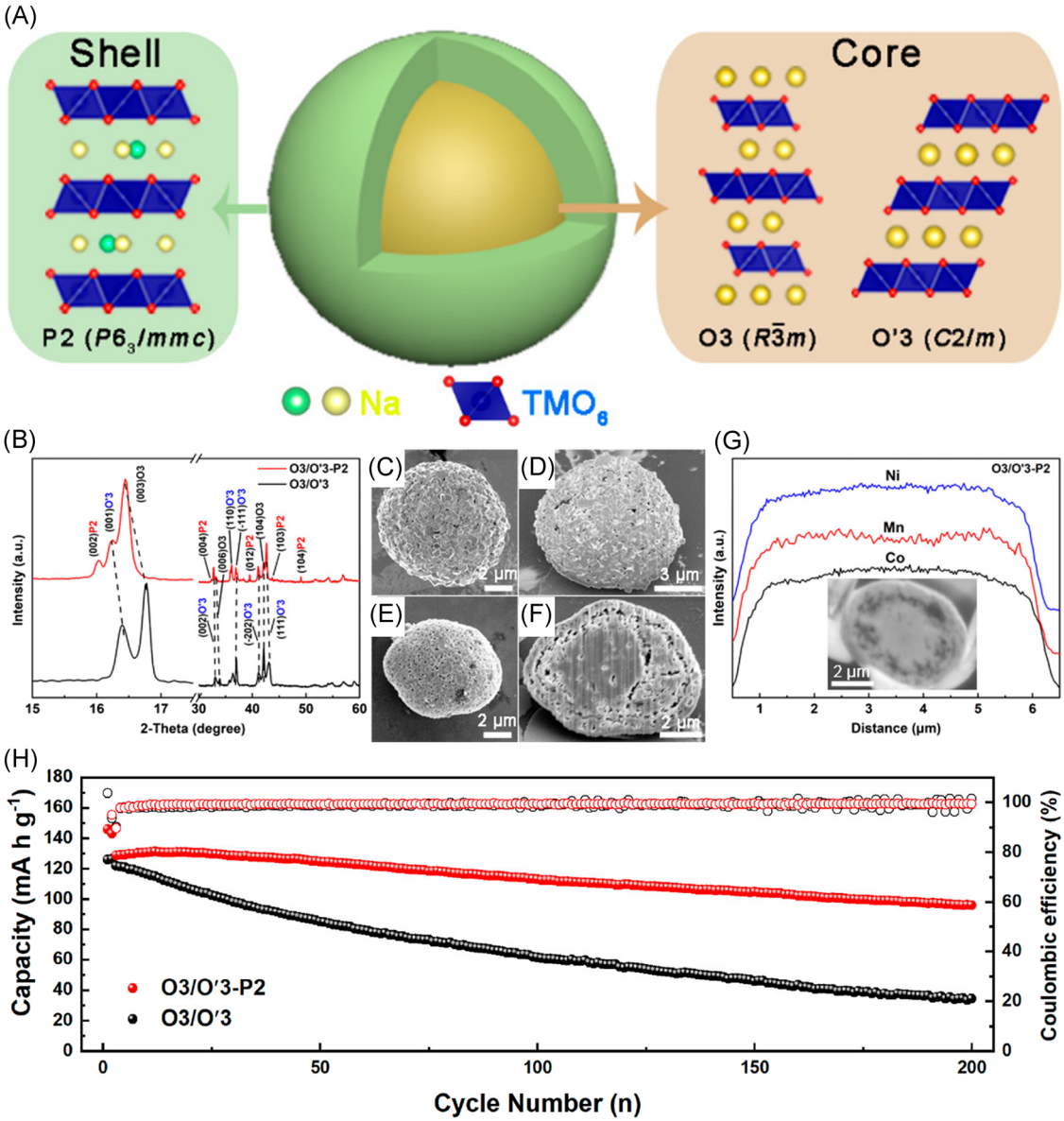

FIGURE 5 (A) Schematic of the designed core-shell $Na_{0.8}[(Ni_{0.5}Co_{0.2}Mn_{0.3})_{0.6}(Ni_{0.33}Mn_{0.67})_{0.4}]O_2$ material. (B) XRD of the $NaNi_{0.5}Co_{0.2}Mn_{0.3}O_2$ core (O3-O′3) and O3-O′3/P2 core-shell. (C, D) SEM and cross-sectional SEM of the core-only and (E, F) core-shell secondary particles. (G) EPMA line scan probing the heterogeneous TM distribution. (H) Capacity retention of the core material compared to the core-shell material. Reprinted (adapted) with permission from Reference [75]. Copyright 2020, American Chemical Society. EPMA, electron probe X-ray microanalysis; SEM, scanning electron microscopy; TM, transition metal; XRD, X-ray diffraction

In comparison to the O3–O′3 $NaNi_{0.5}Co_{0.2}Mn_{0.3}O_2$ core material, the triphasic core-shell material demonstrated higher reversible capacity (146 vs. 125 mAh/g), rate capability, and capacity retention (75% vs. ~27%). The composition of the precursor was controlled by altering the transition metal sulfate solution composition part way through the coprecipitation reaction (Ni:Co:Mn in 5:2:3 molar ratio in the core, 1:0:2 in the shell). The designed core-shell morphology and heterogeneous transition metal composition was investigated after calcination with line-scans of cross-sectioned secondary particles by scanning electron microscopy (SEM) and electron probe X-ray microanalysis (EPMA). The EPMA line scan (Figure 5G) only weakly indicates Mn enrichment and Co-deficiency at the surface, which could be a result of the large volume of interaction created by the electron beam limiting the spatial resolution, and/or interdiffusion of the TM species during the calcination processes. Still, the circular cracks/voids in the composite material near the surface (Figure 5F) suggest that significant radial heterogeneity exists within individual particles. Core-shell LTMO materials are well established in LIB positive electrodes,[76] so the core-shell structure is still plausibly assumed as designed based on the similar methods used in this study. Additionally, the presence of the P2 phase and the O3-O′3 phase in separate areas of an individual secondary particle was observed by atomic resolution high-angle annular dark-field scanning transmission electron microscopy (HAADF-STEM). XRD measurements indicated relatively lower layer expansion during charging in the triphasic material compared to the biphasic material, which was attributed to compression caused by the P2 shell and suppression of crack formation.

The spatial resolution of the characterization techniques (cross-sectional SEM/EMPA and HAADF-STEM) used by Chen and coworkers is critical to evaluate whether the distribution of phases and elements within individual secondary particles is prepared as designed. The synthesis strategy to prepare a P2 shell surrounding an O3-O′3 core employed by Chen and coworkers hinges on the compositional heterogeneity of the TMs and has been thoroughly demonstrated through the coprecipitation technique in LIBs but rarely in SIBs.[76] The overall composition of the designed core-shell material if fully sodiated ($Na_{0.987}Ni_{0.433}Co_{0.12}Mn_{0.447}O_2$ assuming Ni^{2+}, Co^{3+}, and Mn^{4+}), would be predicted to form a single O3 phase based on the cationic potential and sodium content. The simultaneous increase of cationic potential associated with Mn^{4+} concentrated at the surface paired with lower sodium content ($Na_{0.8}$) promotes the formation of the P2 structure, which is key to the enhanced electrochemical properties of the triphasic, heterogeneous material.

A similar synthetic strategy was utilized by Rahman and coworkers to prepare a biphasic electrode with composition $Na_{0.9}Cu_{0.2}Fe_{0.28}Mn_{0.52}O_2$.[85] The authors assigned the structure as a combination of O3 and P3 phases based on the XRD pattern, though detailed structure refinement was not performed. Through manipulation of the composition of the transition metal solution during the coprecipitation synthesis of the mixed hydroxide precursor, different distributions of the transition metals throughout the particle are expected. A sample in which iron and manganese were first completely precipitated as hydroxides, followed by the complete precipitation of copper was characterized by transmission X-ray microscopy (TXM) after solid state reaction. TXM allows for the correlation of the absorbance in individual voxels with specific elements by careful control of the X-ray energy to be just above and below each of the transition metal elements K-edges. The elemental information from each voxel was represented in three dimensions to visualize the transition metal homogeneity throughout an individual secondary particle (Figure 6). Analysis of the absorption correlation tomography data indicated that only 37% of voxels had indications of all three transition metals, and that these voxels were largely located in the bulk of the secondary particle. In contrast, over 30% of voxels contained only a single transition metal element and the remainder of voxels were of binary TM combinations. These unary and binary voxels were predominant at the surface of the particle. The TXM analysis of the pristine material demonstrates the highly heterogeneous distribution of transition metals within the secondary particle, especially at the surface. The heterogeneous, biphasic $Na_{0.9}Cu_{0.2}Fe_{0.28}Mn_{0.52}O_2$ material demonstrated negligible loss of the initial 125 mAh/g discharge capacity over 100 cycles at a current of 10 mA/g in the 2.0–4.0 V window, with a high 1st cycle Coulombic efficiency of 99.3%. The excellent electrochemical performance of the heterogeneous biphasic $Na_{0.9}Cu_{0.2}Fe_{0.28}Mn_{0.52}O_2$ material was hypothesized to be a result of the synergistic effect of the high capacity O3 phase and good Coulombic efficiency of the second phase. Through a combination of soft and hard X-ray absorption spectroscopy (XAS), and X-ray Raman spectroscopy the authors demonstrated that the electrochemical reaction mechanism varied from the surface to the bulk as a result of the heterogenous distribution of transition metals.

Additional TXM analysis was performed on the material after 400 cycles, which indicated that there was substantial reduction in the ternary metal association driven by TM segregation and manganese migrating from the bulk to the surface during cycling. This interpretation of TM distribution change after cycling relies on the representativeness of the individual particles

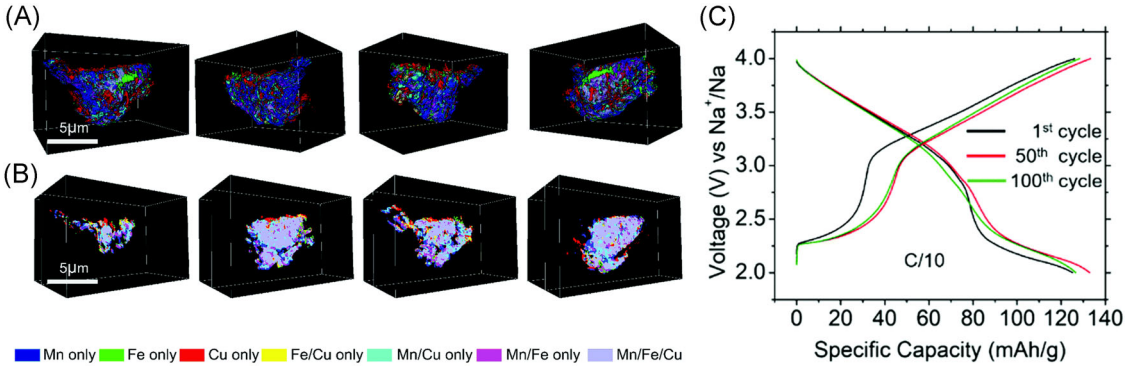

FIGURE 6 (A) X-ray tomography 3D association maps in different orientations indicating the prevalence of unary and binary TM associations at the surface. (B) 2D slices at various depths of the secondary particle showing the different associations between bulk and surface. (C) Voltage profiles of the heterogeneous biphasic $Na_{0.9}Cu_{0.2}Fe_{0.28}Mn_{0.52}O_2$ electrode demonstrating high 1st cycle Coulombic efficiency and capacity retention over 100 cycles. Reproduced with permission from Reference [85]. Copyright 2018, Royal Society of Chemistry. 3D, three dimensional; TM, transition metal

in comparison to the statistical distribution across the entire electrode, which may be critically important.[105] This principle is also important to consider in regard to other properties such as structure and orientation, not only composition. With advanced characterization techniques such as TXM, multiple measurements to determine statistical variation must be balanced against the time and other difficulties required for each measurement. Application of complementary techniques that can determine similar information at longer length scale can provide statistical average properties, which can be a useful means to balance such experimental difficulties.

3.2.2 | Design and characterization of microscale phase interfaces

The design and characterization of multiphase positive electrode materials with microscale phase interfaces should concentrate on the spatial distribution of the transition metal elements and phases within particles, as well as the effect of the phase interaction on the electrochemical properties. When the level of synthetic control allows, the mechanisms of microscale interactions can be effectively studied by modifying the spatial distributions of elements/phases. To comprehensively study a two-phase system where both phases can be prepared in isolation, a simple mixture of the pure phases should be compared to the two phases as integrated into individual secondary particles with the same overall stoichiometry, as well as the isolated pure phases.[106] Using mixtures and pure phases as benchmarks will deconvolute the electrode-scale effects from those that affect individual particles. At the secondary particle scale, the spatial distribution of the phases/elements can then be altered. A sample with homogeneous distribution of elements and/or phases could be compared to a core-shell material with the same overall composition to study the effect of the cathode-electrolyte interface and transport properties near the surface.[107] If the core-shell compositions are swapped (i.e., the original shell becomes new core, original core becomes new shell), this further elucidates the effect of surface phase properties on performance and simultaneously alters the mechanical coupling between phases within the particle. To study electrode materials with heterogeneous structure and composition, researchers must utilize methods that have sufficient spatial resolution to observe differences within individual secondary particles. Precise spatial control of sample synthesis through techniques such as coprecipitation, when combined with advanced microscopy techniques such as TXM and HAADF-STEM provide a valuable avenue to design and characterize high-performance LTMOs for SIBs.

3.3 | Nanoscale phase interfaces

LTMOs with nanoscale interfaces at the surface and/or in the bulk often demonstrate notably enhanced electrochemical properties such as cyclic stability, power density, and energy density.[22,70–72,79–84,108,109] The location, quantity, and properties of these interfaces dictates their effect on performance.

3.3.1 | Nanoscale surface interfaces

Surface coatings with thickness <100 nm can significantly modify the surface properties of LTMOs by altering the surface structure and composition, while

simultaneously only composing a small percentage of the material (often 5% or less by weight).[110] These nanoscale coatings can improve air stability, structural and thermal stability, suppress TM dissolution, enhance sodium ion transport, and modify reaction with the electrolyte.[22,70–72,74,94,111] Surface coating methods such as sol-gel and wet chemical process,[73,86,89,112] melt-impregnation,[90] and magnetron sputtering[113] can all provide significant performance benefits, but may not achieve the high degree of conformality and thickness uniformity provided by more complex techniques such as atomic layer deposition (ALD).[70–72,94] Surface phases may also spontaneously (partially) segregate from the bulk.[22,91,92]

Characterization of these surface phases is usually performed through a combination of surface sensitive and/or high spatial resolution techniques such as X-ray photoelectron spectroscopy (XPS), electrochemical impedance spectroscopy (EIS), and electron microscopy (SEM/TEM/STEM) paired with composition-sensitive techniques of electron energy-loss spectroscopy (EELS) and energy dispersive X-ray spectroscopy (EDS) or EPMA. These techniques allow for determination of surface layer composition, thickness and uniformity, oxidation state, and transport properties.

Liquid-based coating processes

Many examples of coating processes utilize the homogeneous nature of liquid in attempt to uniformly distribute coating materials onto the surface of pre-formed electrode particles. Liquid based processes have the benefit of versatility in choice of coating compound, since LTMO electrode materials are poorly soluble in most solvents and can tolerate high temperatures, allowing solvents to evaporate or melt/resolidify without damage to the electrode material. The simplicity of the liquid-based coating technique is an additional benefit. Coatings (including, but not limited to) of $NaPO_3$,[90,114,115] $NaTi_2(PO_4)_3$,[86,116] $Na_2Ti_6O_{13}$,[117] $NaCaPO_4$,[87] $AlPO_4$,[89] Al_2O_3,[73,118] carbon,[112] $Mg_{1-x}Ni_xO$[88] have all been demonstrated using liquid based coating techniques to enhance the electrochemical properties of various LTMOs as positive electrodes for SIBs.

The synthesis methods utilized by Deng and coworkers to prepare P2-type $Na_{0.65}Mn_{0.70}Ni_{0.16}Co_{0.14}O_2$ coated with $NaTi_2(PO_4)_3$ (referred to as NMNCO@NTP) exemplify the liquid based coating strategy (Figure 7).[86] The uncoated NMNCO is initially prepared by sol-gel method by dissolving sodium, manganese, nickel, and cobalt acetates in water and combined with citric acid under stirring and heat, then dried and calcined form the P2 structure. A subsequent sol-gel process dispersed NMNCO in ethanol and tetrabutyl titanate solution, which was then slowly mixed with an aqueous solution of Na_2CO_3 and $NH_4H_2PO_4$ and heated until the solvents evaporated. The NMNCO coated in the $NaTi_2(PO_4)_3$ precursors then underwent a secondary calcination step to form the NMNCO@NTP composite electrode. TEM and EDS were used to confirm the uniform distribution of Ti and P, and the altered lattice fringes at the surface of individual particles confirmed the presence of the NTP coating. A number of benefits were associated with the NTP coating. Samples with 1, 3, and 5 wt% of NTP coating were prepared. The 1 wt% sample was not uniformly coated, and the 5 wt% coating was excessively thick. An optimized 3 wt% of NTP coating resulted in reduced volume expansion and suppressed P2-O2 transition during charge compared to the uncoated material, as observed by TEM and operando XRD. The enhanced structural stability could explain the superior capacity retention (88.3% vs. 42.8% after 100 cycles) of the coated material. EIS measurements of the coated and uncoated

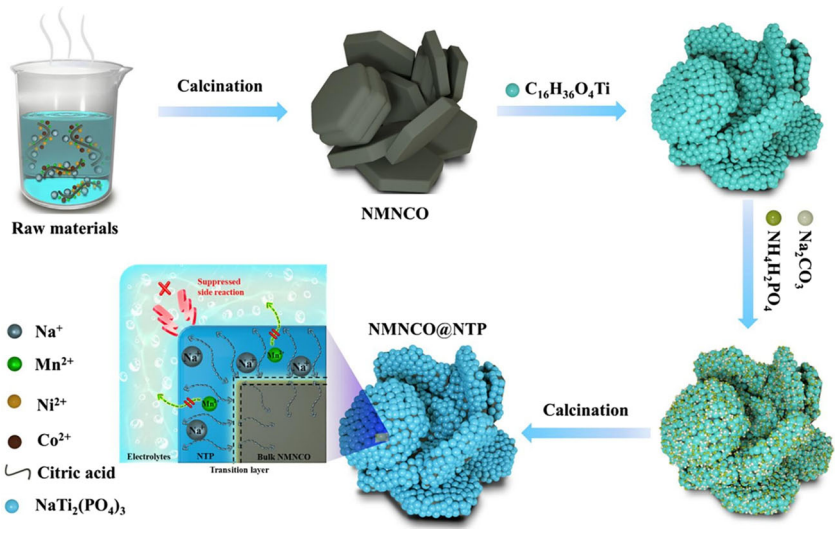

FIGURE 7 Liquid-based (sol-gel) process for synthesis of composite P2-$Na_{0.65}Mn_{0.70}Ni_{0.16}Co_{0.14}O_2$@$NaTi_2(PO_4)_3$. Reprinted from Reference [86] with permission. Copyright 2021, Elsevier

material were fitted to an equivalent circuit model and found that the coated material had less than half the interfacial charge transfer resistance and double the sodium diffusivity. In combination with the known high Na^+ diffusivity of the NASICON structure of NTP, the superior rate performance of the coated material (83 mAh/g coated vs. 25.1 mAh/g uncoated at 2400 mA/g current) is rationalized.

Other researchers have demonstrated similar performance benefits with slight variations in sample preparation, depending on the coating and electrode chemistry. Biologically inspired $NaCaPO_4$ coating on P2-$Na_{2/3}Ni_{1/3}Mn_{2/3}O_2$ (NNMO) was able to scavenge HF and H_2O from the electrolyte, protecting the electrode material from exfoliation during cycling as well as suppress oxygen evolution during heating for enhanced safety.[87] Only 0.5 wt% of the coating was necessary to enhance discharge capacity retention to 74% after 200 cycles in 2.5–4.3 V, compared to only 31% for the bare material. In another work, an $Mn_{1-x}Ni_xO$ coating on similar NNMO material was shown to provide similar protection against HF attack even during cycling at 60°C.[88] P2-$Na_{0.7}MnO_2$ coated with 5 wt% of $AlPO_4$ demonstrated superior rate performance and cyclic stability compared to the bare material (92.4% coated vs. 62.4% bare after 100 cycles).[89] SEM observations showed the coating introduced significant roughness to the surface, and EDS mapping in TEM observation showed the nonuniform thickness of the coating (Figure 8). Only 3 wt% of $AlPO_4$ coating resulted in incomplete coverage, and 7 wt% was prone to form agglomerates of $AlPO_4$. EIS measurements after 5 and 100 cycles showed the 5 wt% coated sample had lower charge transfer resistance than the uncoated sample. In a separate work, the same $Na_{0.7}MnO_2$ material was coated with $NaPO_3$ by mixing the electrode material with $NH_4H_2PO_4$ (melting point = 190°C) and heating to 300°C to cause the decomposition reaction.[90] The $Na_{0.7}MnO_2$@$NaPO_3$ delivered a remarkable 95.5 mAh g^{-1} discharge capacity at the high current density of 3000 mA g^{-1}, which is 58% of the capacity delivered at low 10 mA g^{-1} current and significantly better than the 34.3% shown for the uncoated material at the same rates. The enhanced rate performance was also investigated using EIS, which indicated lower charge transfer resistance and higher sodium diffusivity.

These examples of LTMO positive electrode materials combined with liquid based coating processes have many properties in common—enhanced cycling stability and power density. The surface protection granted by the chemically stable and fast-ion-conducting coatings mitigates mechanical and structural degradation during cycling and shields the electrode surface from the corrosive organic electrolytes. The wide range of coating chemistries available and simplicity of the liquid coating process make it a versatile technique for enhancing electrode materials. However, the amount of coating material must be carefully optimized to ensure

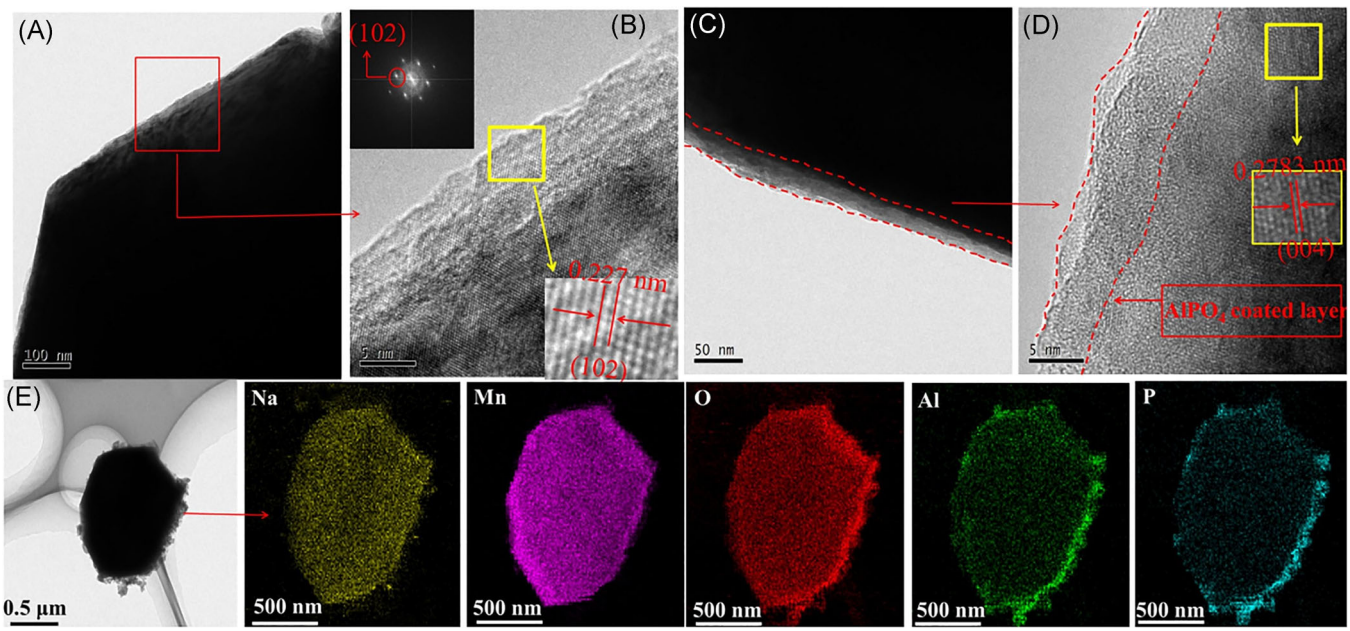

FIGURE 8 (A–D) TEM images showing the amorphous $AlPO_4$ coated $Na_{0.7}MnO_2$ and (E) corresponding EDS mapping showing the nonuniformity of the coating. Reprinted from Reference [89], with permission from Elsevier. EDS, energy dispersive X-ray spectroscopy; TEM, transmission electron microscopy

complete coverage and simultaneously avoid agglomeration or excessive thickness. Toward the goal of uniform coating with optimized thickness, characterization methods with high spatial resolution such as electron microscopy (SEM/TEM/STEM) paired with element sensitive techniques (e.g., EDS mapping) are invaluable to rationalize the observed changes in performance. Characterizations which allow surface processes to be investigated, such as EIS provide valuable information about the effect of the modified electrode-electrolyte interface.

Spontaneous surface phase segregation

The simplicity of the liquid-based coating techniques is a strength, but still more complex than the formation of coatings spontaneously from thermodynamically favorable processes during the typical calcination process. Certain electrode compositions have been observed to spontaneously segregate certain elements to their surface, forming surface oxides with remarkably different properties than the composition in the bulk.[22,91,92] This is in contrast to the kinetic control of element distribution employed in coprecipitation or surface coating methods. Thermodynamically driven surface segregation phenomenon result from differences in free energy for the segregating species between the surface and bulk to minimize the total free energy.[22,119] Coatings formed in such a manner require no additional processing, which is very convenient for practical application. Materials such as ZnO,[22] ZrO_2,[92] and spinel-like Ti(III) oxide[22] have been observed to form surface layers spontaneously on several sodium based LTMOs using conventional calcination processes. Similar surface layers have been noted for lithium-based oxide positive electrodes.[120–122] An important consideration for this technique is that it is likely to also introduce the segregating species in some quantity in the bulk, which may or may not be desirable. Additionally, since the thermodynamic driving forces for surface segregation are dictated by the specific chemistry of the composition, the coating material and electrode material combinations are restricted and may be difficult to control.

Guo and coworkers demonstrated the spontaneous formation of a spinel-like Ti(III) oxide on the surface of $NaMn_{0.8}Ti_{0.1}Ni_{0.1}O_2$ (NMTN) with significantly enhanced performance compared to the O′3 type $NaMnO_2$ (NM).[22] Using atomic resolution HAADF-STEM paired with EELS chemical mapping, the approximately 2 nm thick surface layer was identified to be composed primarily of titanium oxide (Figure 9). The surface layer was observed to be highly uniform and continuous for all particles examined. Disorder in the form of Ti and O vacancies at the surface as suggested by the EELS spectra and HAADF-STEM images was suggested to possibly result in increased conductivity of the interface. XRD revealed that the substitution of Ti/Ni for Mn also modified the long-range structure from a single O′3 phase in NM to a biphasic O′3-P2 combination with 59.5% P2% and 40.5% O′3 by weight in NMTN. STEM investigation of over 20 particles revealed that the Ti(III)-spinel layer only existed at the surface in contact with the O′3 phase, and that the P2 phase was found only at the core of particles, suggesting an overall P2@O′3@spinel structure with both microscale (P2@O′3) and nanoscale (O′3@spinel) phase interfaces. The NMTN sample experienced no change in long-range structure after 3 days exposure to moist air in contrast to the significant change seen in the NM material that intercalated water, suggesting that the Ti-spinel surface layer protected against H_2O intercalation. Differential scanning calorimetry (DSC) further supported the value of the coating, where the charged NMTN sample released less heat (101.8 J/g) at a higher onset temperature (283°C) compared to NM (181.2 J/g at 255°C). Additionally, the NMTN prevented Mn dissolution based on the inductively coupled plasma mass-spectroscopy (ICP-MS) observation of manganese in the sodium anode cycled with the NM material but not NMTN. Finally, the electrochemical performance was evaluated, revealing the NMTN had enhanced cyclic stability (86% for NMTN and 36% for NM after 50 cycles) and four times greater capacity at 1000 mA/g than NM. Clearly, the spontaneously formed surface layer of spinel-like Ti(III) oxide on NTMN and its biphasic P2@O′3 structure results in a myriad of performance benefits while requiring no significant additional effort to form compared to NM. The observation of many particles that was performed in this study is essential, as the nature of HAADF-STEM and other high-resolution techniques yields local information. If local observations are used to interpret behavior at larger length scales, then it is critical that the local information is statistically applicable at the larger scale.

Utilizing similar synthesis techniques, Zhang and coworkers investigated $Na_{0.66}Ni_{0.33}Mn_{0.67}O_2$ (NNM), Ni/Zn substituted $Na_{0.66}Ni_{0.26}Zn_{0.07}Mn_{0.67}O_2$ (NNZM), and $Na_{0.66}Ni_{0.26}Zn_{0.07}Mn_{0.67}O_2$ coated with ZnO by spontaneous formation during calcination (NNZM@0.06ZnO) and contrasted with ZnO coating via mechanical milling (NNZM/0.06ZnO).[91] The experiment design rationally separates the effect of Zn doping in the bulk from the surface coating by comparing NNM and NNZM ($Ni + Mn + Zn = 1$), where no ZnO coating is observed. The effect of coating formation process is then investigated by adding Zn such that $Ni + Mn + Zn > 1$ (spontaneous NNZM@0.060ZnO and milling coated NNZM/0.06ZnO). The use of transition metals with stoichiometric sum greater than one (vs. the unmodified material) is unique in

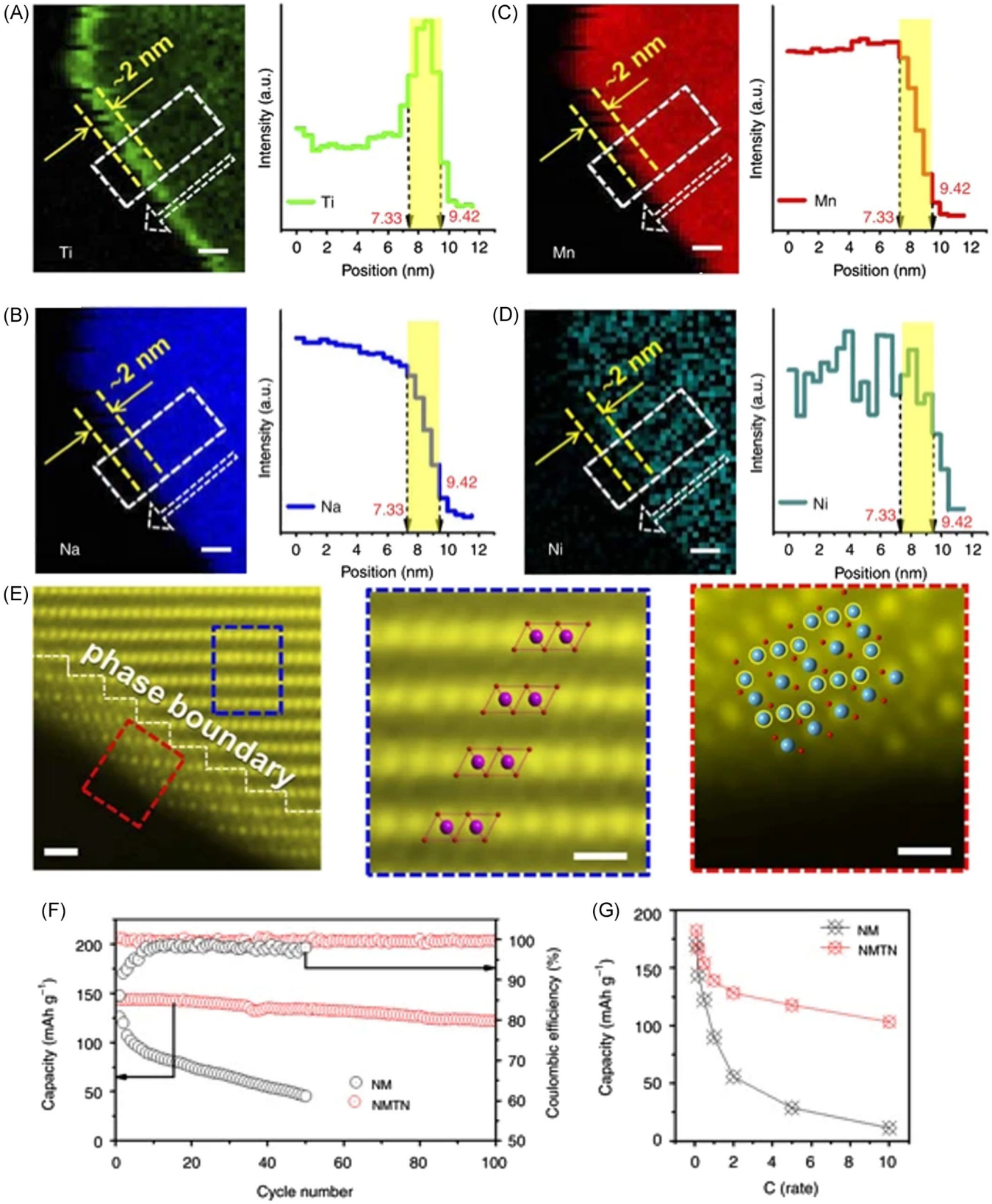

FIGURE 9 (A–D) EELS mapping near the surface of the NMTN electrode surface showing Ti enrichment. (E) HAADF-STEM showing the interface between the spinel-like coating and layered bulk structure. (F, G) Comparison of cyclic stability and rate performance between the coated NMTN and bare NM material. Adapted from Reference [22] with permission under Creative Commons Attribution 4.0 International Public License. EELS, electron energy-loss spectroscopy; HAADF-STEM, high-angle annular dark-field scanning transmission electron microscopy; NM, $NaMnO_2$; NMTN, $NaMn_{0.8}Ti_{0.1}Ni_{0.1}O_2$

this material compared to the titanium oxide coating previously discussed. Comparison of the voltage profiles of the NNZM material and the Zn-free NNM suggests that Zn doping can disrupt Na/vacancy ordering processes that occur during charge in NNM. Zn doping (NNZM) generates a slight improvement in capacity retention after 100 cycles compared to NNM (63.4% vs. 50.8%, respectively). The spontaneously coated NNZM@0.06ZnO sample demonstrates significantly enhanced capacity retention of 83.7%, while NNZM/0.06ZnO coated by mechanical milling demonstrates worse capacity retention (57.1% at 100 cycles) than the uncoated NNZM, highlighting the importance of the processing method for coating formation on the performance. The spontaneous ZnO coating formation mechanism was investigated by in situ high-temperature XRD, revealing that before complete sodiation Zn^{2+} could mostly be accommodated in the P2 TM layer. As sodium content increased, Ni^{2+} was preferentially stabilized in the P2 phase while ZnO segregated. NNZM@0.06ZnO exhibits improved air stability, reduced reactivity with electrolyte, and more reversible structural transformation during charge/discharge.

P2-$Na_{0.67}Mn_{0.7}Fe_{0.2}Co_{0.1}O_2$ with Zr^{4+} doping and ZrO_2 coating was investigated by Kong and coworkers through the addition of zirconium tertbutoxide to the sol-gel synthesis (Mn + Fe + Co + Zr > 1) used to prepare the Zr-free material (Mn + Fe + Co = 1).[92] A nonuniform ZrO_2 coating thickness was observed, but still resulted in enhanced capacity retention compared to the uncoated material, which was attributed to reduced reaction with the electrolyte and enhanced structural stability from Zr^{4+} doping. The nonuniformity of the ZrO_2 coating compared to the previous examples suggests that the coating and bare material composition may be an important factor in how these interfaces form.

Spontaneously formed coatings are advantageous in that they require no additional processing and can form highly uniform coatings under certain conditions. The uniformity and thickness of the coatings may not be trivial to control, however. Some extent of doping of the segregating species is inevitably expected, which may or may not be beneficial. Further investigation is warranted to understand the role of composition and other processing variables to develop design strategies for controlled spontaneous coating formation.

Self-limiting conformal coatings

ALD and the closely related molecular layer deposition (MLD) techniques are of great interest because they can form highly conformal coatings of uniform thickness on the complex surface geometries of electrode particles.[123–125] The properties of uniformity and conformality arise from the self-limiting nature of the ALD and MLD chemical reactions. In the idealized conception of ALD and MLD, a precursor gas (e.g, tetramethyl aluminum or TMA) is introduced to a controlled atmosphere environment and adsorbs to sites on the surface of the electrode material. When the surface is saturated with the adsorbed precursor, the system is purged and a different gas chemistry is introduced (e.g., water). The different gas will react with the adsorbed precursor from the previous step, leaving a single atomic or molecular layer (e.g, Al_2O_3) on the surface of the electrode material and the gaseous byproducts (e.g., methane) and excess reactant gases can be purged. Every repetition of the alternating gas chemistries will generate a single additional monolayer, allowing for precise thickness control. The self-limiting nature of the surface reaction promotes conformality of the coating since the growth per cycle should be the same everywhere due to the adsorbed precursor availability limiting the reaction. Consequently, ALD and MLD can theoretically result in superior control over coatings compared to other methods. An additional strength is that this process can often be performed at low temperature (only 150°C for Al_2O_3),[72] which can limit diffusion of the coating chemistry into the bulk. Maintaining the coating species at the surface allows for the bulk properties to remain unmodified, unlike the spontaneous coating process. The advanced control provided by ALD and MLD is at the cost of more complex processing equipment and exotic precursor chemistry compared to liquid based or spontaneous coatings. As a result of film growth one layer at a time, thick coatings can be impractical due to the slow growth rate. It is also possible that deviations from ideal self-limiting behavior with constant growth per cycle occur, leading to some nonuniformity in the coating. Nonetheless, ALD and MLD have been demonstrated as powerful techniques to enhance the performance of LTMO positive electrodes for SIBs. Coatings such as Al_2O_3,[70–72,94,95,126] alucone (organic-aluminum hybrid polymer),[93] Fe_2O_3,[111] ZrO_2,[126] and TiO_2[126] have been demonstrated to enhance the performance of LTMOs for SIB application.

Al_2O_3 is the most extensively studied ALD coating for SIB LTMOs currently, which is likely due to the high reaction enthalpy of the TMA/H_2O reaction and efficient, strong self-limiting behavior that make Al_2O_3 a good model system to facilitate scientific investigation.[123,127] Al_2O_3 coatings deposited via ALD have been shown to promote air stability,[71,94] prevent exfoliation,[72] stabilize the structure[94] and electrode-electrolyte interface,[70] alter cathode-electrolyte interphase composition,[72] and reduce interfacial resistance.[70,72,95] Alvarado and coworkers used XPS to identify that a 1 nm Al_2O_3 ALD coating directly on prepared electrodes of $Na_{2/3}Ni_{1/3}Mn_{2/3}O_2$

altered the cathode electrolyte interphase composition compared to uncoated material, with significant effect on the electrochemical performance (Figure 10A,B).[72] Superior capacity retention and superior rate performance up to C/2 was associated with the coating. Using XPS, the composition of the surface was analyzed at different voltages and cycle numbers for the coated and bare samples (Figure 10C). The coated material was revealed to form more NaF, and polymeric species such as poly(ethylene oxide) which could provide protection

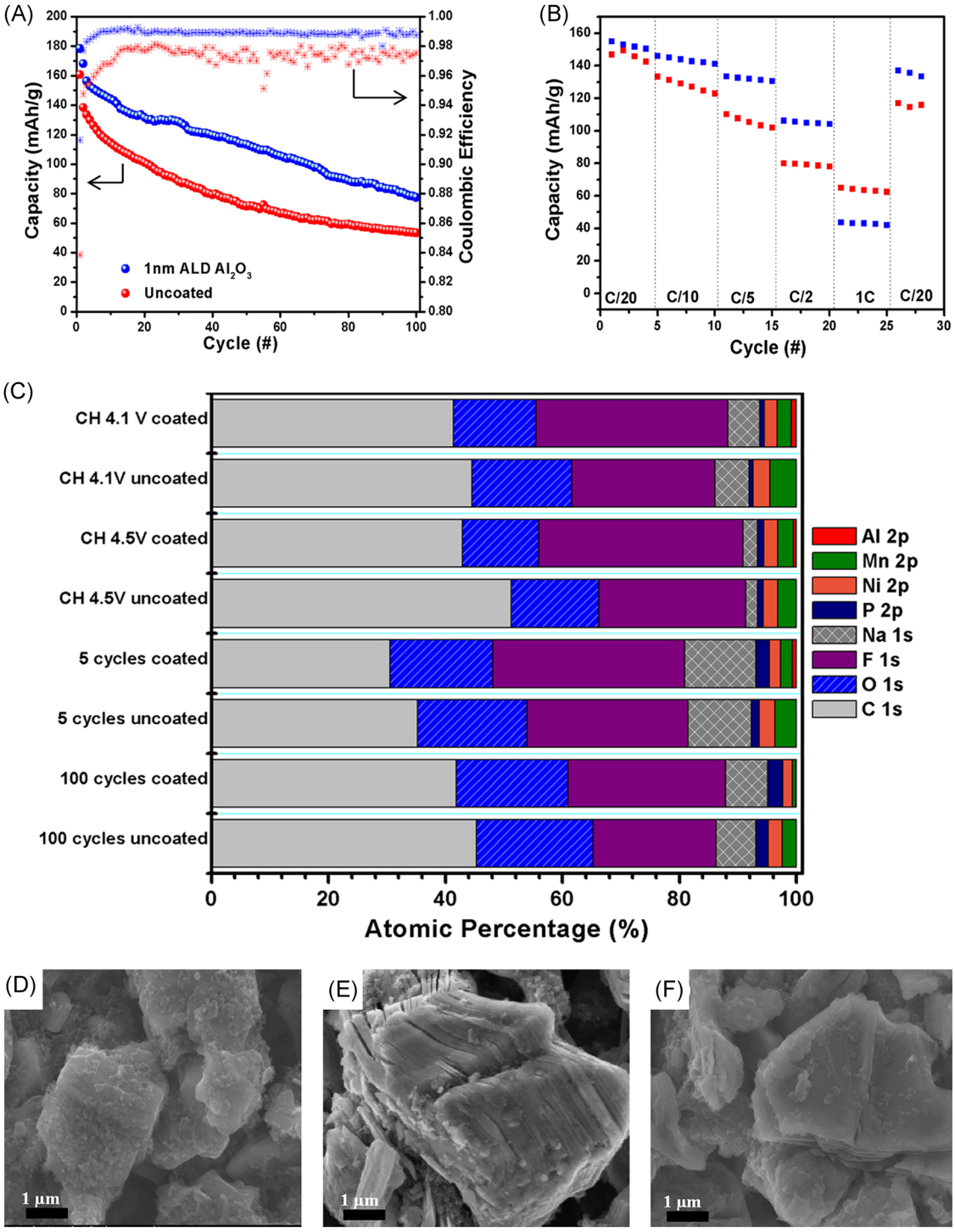

FIGURE 10 (A) Cycle stability and coulombic efficiency, (B) rate performance, (C) cathode-electrolyte interphase composition at different states of charge with and without ALD Al_2O_3 coating, (D) SEM of the pristine uncoated P2-$Na_{0.67}Ni_{0.33}Mn_{0.67}O_2$ electrode. (E, F) SEM of the uncoated and coated material after 100 cycles, respectively. Reprinted (adapted) with permission from Reference [72]. Copyright 2017, American Chemical Society. ALD, atomic layer deposition; SEM, scanning electron microscopy

against HF formation while maintaining flexibility to accommodate volume expansion during cycling. This could explain the high degree of exfoliation seen in the uncoated sample compared to the Al_2O_3 coated material (Figure 10D–F). The importance of the ability of the ALD coating to enhance the surface chemical stability and also handle the mechanical stresses of the electrode material are evident from these results.

Another key property of coatings prepared by ALD is their electronic and ionic conductivity to facilitate high power density. Kaliyappan and coworkers prepared ultrathin coatings (~0.2–0.3 Å) of TiO_2, Al_2O_3, and ZrO_2 on P2-$Na_{0.66}Mn_{0.54}Co_{0.13}Ni_{0.13}O_2$ using ALD to compare the transport properties of the different oxides.[126] It was found that the rate performance was improved in the order of $ZrO_2 > Al_2O_3 > TiO_2$ which correlates with the fracture toughness of the oxides. In contrast, the cycle stability was improved in the order $Al_2O_3 > ZrO_2 > TiO_2$ which correlated with their band gap energies. The mechanical and electronic properties of the coating are evidently of high importance to the specific electrochemical performance changes.

Recognizing the importance of flexibility, good transport properties, and high chemical resistance, Kaliyappan and coworkers demonstrated the superiority of an alucone coating using MLD on P2-$Na_{0.66}Mn_{0.9}Mg_{0.1}O_2$ compared to ALD Al_2O_3 coated or bare material.[93] Using TMA as the aluminum source but substituting water for ethylene glycol results in the formation of alucone rather than Al_2O_3. The bare (NMM), Al_2O_3 (Al-NMM), and alucone (Alu-NMM) coated materials all demonstrated approximately equal capacities of 163 mAh/g. However, the alucone coating resulted in a capacity retention of 86% after 100 cycles compared to 71% and 65% for the Al_2O_3 coated and bare material (Figure 11). In addition to the superior first cycle Coulombic efficiency (95.8%) compared to the uncoated sample, Alu-NMM also demonstrated higher sodium ion diffusion coefficient than both Al-NMM and NMM based on the higher slope of the linear feature (Wahrburg line) in the low frequency region of the EIS spectra. This could be explained by the superior transport kinetics through the low density alucone compared to dense Al_2O_3 and lower interfacial resistance compared to the bare material. This study demonstrates that while ALD coating of oxides is the most common, exploration of partially organic coating chemistries has great promise in enhancing electrochemical performance of LTMOs for SIBs.

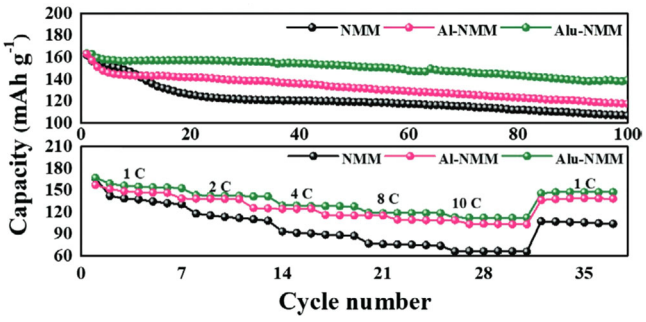

FIGURE 11 (Top panel) Cycle life and (bottom panel) rate performance of bare, Al_2O_3, and alucone NNM coated P2-$Na_{0.66}Mn_{0.9}Mg_{0.1}O_2$. Reproduced (adapted) with permission from Reference [93]. Copyright 2020, Wiley-VCH. NNM, $Na_{0.66}Ni_{0.33}Mn_{0.67}O_2$

Several works have demonstrated the importance of coating thickness on electrochemical properties. The precise control provided by ALD/MLD methods allows for careful study of the thickness effect. O3-$NaNi_{0.5}Mn_{0.5}O_2$ coated with Al_2O_3 in different thicknesses showed that capacity retention was enhanced by coating up to 20 cycles (3 nm), but thicker coatings reduced both rate performance and capacity retention due to the electrical resistance and electrochemical inactivity of the Al_2O_3 film.[94] Increased thickness of coating of Al_2O_3 on $Na_{0.66}Mn_{0.54}Co_{0.13}Ni_{0.13}O_2$ was found to enhance coulombic efficiency and capacity retention over many cycles, but at the expense of reduced rate performance, consistent with the result of the O3-$NaNi_{0.5}Mn_{0.5}O_2$ material.[94,95]

Clearly, ALD and MLD are powerful and precise tools for controlled deposition of varied coating chemistries. These techniques allow for highly conformal and uniform thickness coatings on the complex surface geometry of electrode particles. The primary drawback of the technique is the relatively complex processing compared to simple liquid based or spontaneously formed coatings. Both the chemical nature and thickness of the coating is of significant importance to the properties it can impart. These techniques are a rich area for future research toward high-performance LTMOs for SIBs.

3.3.2 | Nanoscale bulk interfaces

Phase integration at the atomic scale (intergrowth) is able to provide powerful coupling between phases resulting in significant changes to properties and electrochemical performance. However, the intentional synthesis of multiphase materials with this level of phase interaction is nontrivial. Challenges are associated with the elucidation of factors that can promote atomic-scale phase integration. A variety of LTMO materials have demonstrated the intergrowth of nanometer-scale domains of two or more phases in the bulk of individual primary particles.[58,79–84,97,98,128–134] Multiphasic intergrowth in the

bulk of materials can arise in compositions known to form pure, single phases as a result of many different varied parameters, including Na content,[81,82] TM composiiton,[81,98,135] the addition of dopants,[58,79,80,83] varied calcination process (temperature, cooling procedure),[83,84] or combinations thereof.

Design of nanoscale bulk interfaces

The design of atomically intergrown multiphase LTMO SIB materials is rarely discussed in the literature. Many examples of phase intergrowth have been reported, but the explanation of why multiple phases have formed in atomically close contact with one another is scarce. It is widely known that P-type phases tend to form at low sodium content ($0.5 < \mathrm{Na} < 2/3$) and O-type phases at higher Na contents ($2/3 < \mathrm{Na} < 1$), which was rationalized based on the concept of the cationic potential recently.[19] In the case of intermediate Na content (near the $\bar{\Phi}_{\mathrm{Na}} = 0.4065\,\Phi_{\mathrm{cation}} + 1.572\,\mathrm{nm}^{-1}$ O3/P2 boundary), it might be expected that phase separation could occur to minimize free energy by forming a combination of Na-poor and Na-rich phases in proportion consistent with the overall Na composition. For example, in the case of overall composition $Na_{0.8}TMO_2$, a balance could occur from 0.6 P2-$Na_{2/3}TMO_2$·0.4 O3-$NaTMO_2$. Depending on the TM composition and their energetically favored oxidation states, deviation of the TM composition within a phase from the overall composition could also be expected. Consider $Na_xNi_{x/2}Mn_{1-x/2}O_2$ designed to contain entirely Ni^{2+} and Mn^{4+}. A two-phase mixture with this overall composition could occur from $z\mathrm{Na}_{2/3}\mathrm{Ni}_{1/3}\mathrm{Mn}_{2/3}\mathrm{O}_2\cdot(1-z)\mathrm{NaNi}_{1/2}\mathrm{Mn}_{1/2}\mathrm{O}_2$ (if $2/3 \le x \le 1$), which are known to form the P2 and O3 structures, respectively. This system is predicted based on the cationic potential to transition from O3 to P2 at $x \approx 0.82$ ($Na_{0.817}Ni_{.408}Mn_{0.592}O_2$), which is consistent with experimental observations of P2 $Na_{0.8}Ni_{0.4}Mn_{0.6}O_2$ and O3 $Na_{0.9}Ni_{0.45}Mn_{0.55}O_2$.[82,136] If the overall Na content is increased without altering the TM composition ($Na_yNi_{x/2}Mn_{1-x/2}O_2$, $y > x$) the excess positive charge must be compensated by the formation of Mn^{3+} or TM vacancies, and a decrease in Na content ($y < x$) will require Ni^{3+} formation or oxygen oxidation/vacancies. Such changes to charge compensation could result in structural distortion (from Jahn–Teller active Ni^{3+}/Mn^{3+}) or the formation of impurity phases (e.g., NiO), which could affect performance. If the TM composition is varied while the Na content is held constant ($Na_xNi_yMn_{1-y}O_2$) the charge compensation will be forced to deviate from the designed Ni^{2+} and Mn^{4+}. Similar strategy has been succesful for the design of atomically integrated 'layered-layered-spinel' composite positive electrodes in LIBs.[77,78] Atomic-level phase integration can result from local TM/Na/dopant segregation[83] and the compatible lattice parameters between phases, which commonly integrate along the layering direction[79,80,97] or at the layer edges if the relative orientation of phases is matched.[130,135]

Other than control over the composition, the structure can sometimes be controlled through manipulation of the calcination process.[83,84] The use of different temperatures or cooling procedures can allow high-temperature phases, or transient intermediate phases to be quenched and captured in metastable state at room temperature. Intergrowths formed as a result of varied calcination procedure have the benefit of not altering the composition, which allows for the properties of pure phase samples to be compared to intergrowths without convolution from property changes resulting from the different composition.

Characterization of nanoscale bulk interfaces

A challenge presented by LTMOs with nanoscale bulk intergrowth is the increased difficulty of characterizing nanometer-level heterogeneity that is not accessible through surface-sensitive techniques. This eliminates much of the value provided by surface-sensitive tools used for characterizing nanometer-scale surface interfaces. Near-atomic resolution is necessary to distinguish intergrowth unambiguously from phase mixtures that can readily occur within secondary particles. Often, multiphase LTMOs in the literature lack the characterization required to be clearly assigned as either intergrowth, microscale mixtures, or a combination of the two.[137,138] Consequently, high-resolution microscopy techniques such as TEM and STEM are indispensible tools to distinguish microscale mixtures within secondary particles from more intimate, atomic-level phase integration within primary particles. In high-resolution TEM (HR-TEM), regions of different phases can be indentified through their altered lattice fringes, and electron diffraction measurements can identify the changes in symmetry and interplanar spacing associated with different structures. Depending on the method of synthesis, particles (especially secondary particles) may be too thick for electron transparency and unless they can be thinned using methods such as focused ion beam milling measurements will be limited to smaller particles or the edges of large particles in excessively thick samples. This introduces uncertainty as to whether the observed region of a particle is representative of the particle as a whole. Particle-to-particle variation is another factor that must be considered, so ideally many particles should be examined in thin cross section. In appropriately thin samples the spatial resolution of STEM and complementary EDS/EELS techniques can be sufficient to resolve chemical information of individual

atoms.[139–142] Atom probe tomography (APT) has been effectively used to study the spatial distribution of elements in $Li_{1.2}Ni_{0.2}Mn_{0.6}O_2$ with sub-nanometer resolution in three dimensions.[143] However, we are not aware of any examples of APT applied for the study of SIB materials. Nonetheless, these advanced characterization tools have the potential to access information critical for the understanding of nanoscale heterogeneity in the bulk of LTMOs.

Other than evidence from direct local observation, secondary evidence of intergrowth can present itself through diffraction techniques.[144] When distinct LTMO phases are integrated along the layer stacking direction (*c* axis) and phase interfaces (i.e., stacking faults) occur with sufficient spatial frequency, notable effects on the diffraction pattern arise that can be modeled using software such as DiFFaX[145] and closely related FAULTS.[146] Asymmetrical *hkl*-dependent broadening in the X-ray and/or neutron diffraction patterns is observed, and streaks between the spots in the electron diffraction pattern occur.[147] The effect of intergrowths on diffraction patterns when the phase interface is not along the layering direction may be more difficult to simulate and so direct observation by electron microscopy is still essential. It may also be useful to use different but complementary diffraction techniques (i.e., X-ray and neutron) to leverage the different contrast mechanisms to provide secondary evidence of phase composition or other structural features. Additionally, in situ heating diffraction experiments can be valuable in identifying the range of tempeartures when multiphases are present and whether they remain stable during cooling. The distinction between microscale mixtures and intergrowth can later be made by complementary comparison with microscopy.

Careful combination of complementary characterization methods to identify the short-range and long-range changes in structure, composition, and chemical state is essential for the accurate determination of how nanoscale interfaces in the bulk affect the performance of LTMOs for SIBs.

Synthesis and properties of nanoscale bulk interfaces

Cationic potential manipulation via transition metal and sodium composition. Chen and coworkers demonstrated an O3/P2 (88.4%/11.6%) intergrowth composite with overall composition $Na_{0.9-x}Ni_{0.45}Mn_{0.55}O_2$ when $x = 0.02$, which arose from the slight sodium deficiency compared to pure O3 $Na_{0.9}Ni_{0.45}Mn_{0.55}O_2$.[82] Further sodium deficiency ($Na_{0.86}$) resulted in electrochemically inactive NiO formation simultaneously with the formation of the P2 phase. The O3/P2 biphase ($Na_{0.88}$) demonstrated enhanced capacity retention of 71.1% after 250 cycles at 150 mA/g compared to 38.3% for the pure O3 phase. The biphasic material also showed lower interfacial resistance after 100 cycles and experienced less significant structural transformation after 250 cycles, suggesting the benefit of the intergrowth structure. In lowering the Na content, both Φ_{Cation} and Φ^{-}_{Na} are lowered, moving the system toward the O3/P2 boundary. However, the formation of Ni^{3+} necessary to compensate the Na deficiency appears unfavorable in this composition and others,[148] forming NiO instead. Recently, Xiao systematically examined the $Na_{1-x}Ni_{1-y}Mn_yO_2$ system and had similar results (Figure 12).[96] They further demonstrated that the composition of $Na_{0.85}Ni_{0.4}Mn_{0.6}O_2$ with O3/P2 structure could have the O3/P2 ratio tuned by partial substitution of Mn for other TMs. The different TM substitutions indicated that the general tendency to form the P2 phase was strongest (in descending order) for Mn > Ni > Cu > Fe > Co > Ti.

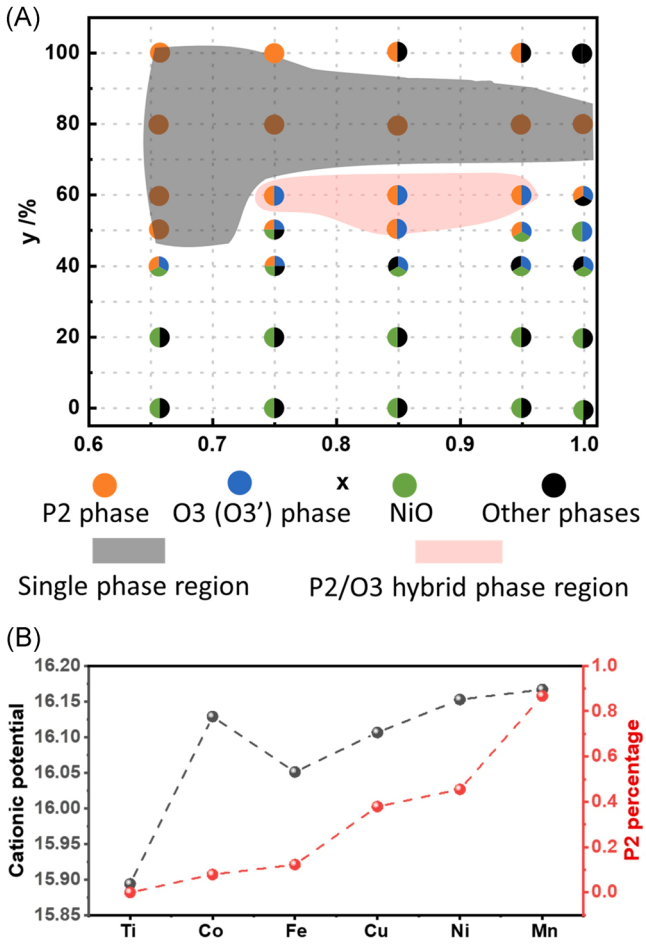

FIGURE 12 (A) Phase diagram of $Na_{1-x}Ni_{1-y}Mn_yO_2$ performed by Xiao et al. identifying the region where O3/P2 intergrowth occurs. (B) Cationic potential and P2 fraction of $Na_{0.85}Ni_{0.4}Mn_{0.5}M_{0.1}O_2$ (M = Ti, Co, Fe, Cu, Ni, Mn). Reprinted from Reference [96], with permission from Elsevier. Copyright 2021, Elsevier

While $Na_{0.85}Ni_{0.4}Mn_{0.6}O_2$ formed 87% P2% and 13% O3, Substitution of Mn with 0.1 Fe, Co, or Ti led to phase fractions of the P2 phase of 12.3%, 7.9%, and 0%, respectively. The calculation of the cationic potential in these ternary compositions is tricky without characterization of the TM oxidation states to determine the charge compensation mechanism for the intermediate Na content of 0.85. Nonetheless, this provides useful insight into which elements may promote the desired phase ratios. These works demonstrate the usefulness of cationic potential manipulation for the generation of phase intergrowth, manipulation of phase ratios, and the importance of considering the favored oxidation states of the transition metals in the design.

Qi and coworkers used a similar strategy of systematic cationic potential variation in $Na_xNi_{0.2}Fe_{x-0.4}Mn_{1.2-x}O_2$ ($0.7 < x < 1$) to generate O3/P2 biphasic material at intermediate Na values between 0.7 and 0.8 (Figure 13).[81] The control of TM stoichiometry simultaneous with the Na composition allows each TM element to remain in a favorable oxidation state of 2+, 3+, and 4+ for Ni, Fe, and Mn, respectively. While the pure O3 phases ($x \geq 0.9$) experienced severe capacity fading and poor rate capability, the samples with significant fraction of P2 ($x = 0.7$–0.8) had a balance of both stability and rate performance. An optimized composition of $Na_{0.78}Ni_{0.2}Fe_{0.38}Mn_{0.42}O_2$ (68.3% O3/31.7% P2) delivered 86 mAh/g of capacity at C/10 rate and was able to retain 90% of its 57 mAh/g capacity after 1500 cycles at 10 C. In contrast with the pure O3 material, the O3/P2 intergrowth material could undergo a fully reversible structural transformation in 2–4 V. The O3 phase reversibly transformed from O3 → P3 → O′3 → P3 → O3 while the P2 phase experienced only a solid solution process with change of lattice parameter, but no phase transformation. The stability and high-rate performance provided by the P2 phase in combination with the high Na content of the O3 phase was suggested as the reason for the superior electrochemical performance of the biphasic electrode. The observed transition between O3 and P2 as the composition varies with intermediate O3/P2 combinations is consistent with the change in Φ_{Cation} and $\bar{\Phi}_{Na}$ crossing the O3/P2 boundary. The samples where $x = 0.76$ and 0.78 are closest to the boundary, which occurs at $x \approx 0.766$ notably have O3/P2 in closer to equal proportion.

While the cationic potential can be a useful predictor of structural preference, in some cases it may be secondary to other factors. Jiang and coworkers reported a P2/P3 composite structure which resulted from substituting Mn for Co in $Na_{0.67}Mn_xCo_yAl_zO_2$.[97] The transition from pure P2 at low Co content to pure P3 at high Co content was observed, with intermediate Co content demonstrating P2/P3 intergrowths. This was evidenced by direct imaging of the change in TM stacking orientation using HAADF-STEM. The P2/P3 (62.2%/37.8%) composite demonstrated suppressed P2→P2′ transition, superior cyclic stability (73% over

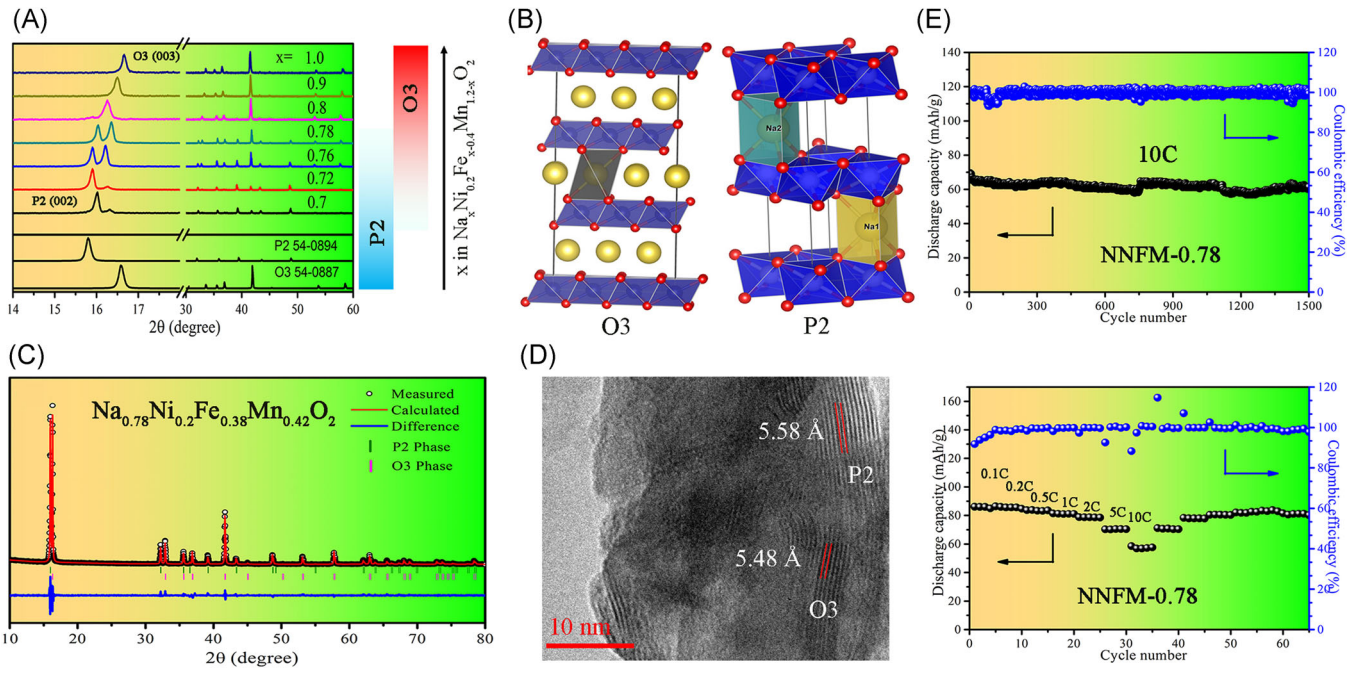

FIGURE 13 (A) XRD of $Na_xNi_{0.2}Fe_{x-0.4}Mn_{1.2-x}O_2$. (B) O3 and P2 structures. (c) Rietveld refinement, (D) TEM, and (E) electrochemical performance of O3/P2 $Na_{0.78}Ni_{0.2}Fe_{0.38}Mn_{0.42}O_2$. Reprinted (adapted) with permission from Reference [81]. Copyright 2017, American Chemical Society. TEM, transmission electron microscopy; XRD, X-ray diffraction

100 cycles vs. 58% for pure P2), and excellent rate capability (83 mAh/g at 1700 mA/g). The dependence of the Co^{3+} ionic potential on spin state, the presence of Jahn–Teller active Mn^{3+}, and the exclusion of the P3 structure from the cationic potential model make this study difficult to interpret solely in the context of ionic potentials. Regardless, any combination of $Mn^{3/4+}$, $Co^{3/4+}$, and Al^{3+} used would predict a P2 phase. The size of Mn and Co ions is very similar when the oxidation states are the same, so the P2/P3 tendency in this system is likely to be dominated by other factors related to the TMs (such as electron configuration) that promote slightly different Na site coordination (i.e., TM-Na-Vacancy in P3 vs. TM-Na-TM and Vacancy-Na-Vacancy in P2). In systems such as this, deeper investigation into the properties of the individual TMs may help explain the observed behavior.

In a similar example, Yan and coworkers prepared P2-$Na_{0.78}Cu_{0.33}Mn_{0.67}O_2$ and substituted Zn^{2+} for Cu^{2+} (ionic potential 27.027 vs. 27.397 nm^{-1}, respectively) to make P2/P3-$Na_{0.78}Cu_{0.26}Zn_{0.07}Mn_{0.67}O_2$.[98] Higher degree of Zn substitution ($Cu_{0.22}Zn_{0.11}$) resulted in ZnO impurity, but complete Zn substitution recovered the P2 structure (P2-$Na_{0.78}Zn_{0.33}Mn_{0.67}O_2$). The Zn substituted P2/P3 cathode had enhanced rate performance and capacity retention similarly to the previous example. It also demonstrated high stability when immersed in water and during high temperature (50–60°C) cycling.

These works demonstrate that while the cationic potential is an important factor in determining structure, other factors related to the nature of the specific transition metal chemistry can generate different stacking sequences (especially in P2/P3 materials) without significant change of the cationic potential.

Nanoscale bulk intergrowth via dopants. Several systems have shown that non-transition metal dopants can promote the formation of nanometer scale phase intergrowth.[58,79,80,99,100,149,150] Utilizing non-TM elements such as Li,[58,79,80,83,149] Mg,[150] Al,[97] Sb,[100] and Sn[99] as dopants can provide notably different size, oxidation state, and electron configuration compared to the TM elements, which could promote the formation of additional phases. Lithium in particular often demonstrates strong tendency to promote additional phase intergrowth. Lithium is known to occupy the TM layer and/or Na layer depending on the material as a result of its comparable size to TM elements and isovalence to Na^+.[79,151,152] This gives lithium the unique property of having the highest ionic potential of the alkali metals, but lower ionic potential than all common transition metal elements, which can result in unique chemistry that strongly depends on the Li environment.

Lee and coworkers explored the $Na_{1-x}Li_xNi_{0.5}Mn_{0.5}O_2$ system, the end members of which ($x = 0$, 1) both form pure O3 phases (Na-O3 and Li-O3, respectively).[79] As Na is exchanged for Li ($x = 0$–0.3), the O3 structure is distorted, forming additional O′3 and P3 phases (Figure 14). The three phases are collectively referred to as {Na-O3} because of their close structural relationship with the original Na-O3 phase. Additionally, peaks corresponding to a P2 phase become evident when $x = 0.2$ and grow at the expense of the {Na-O3} until

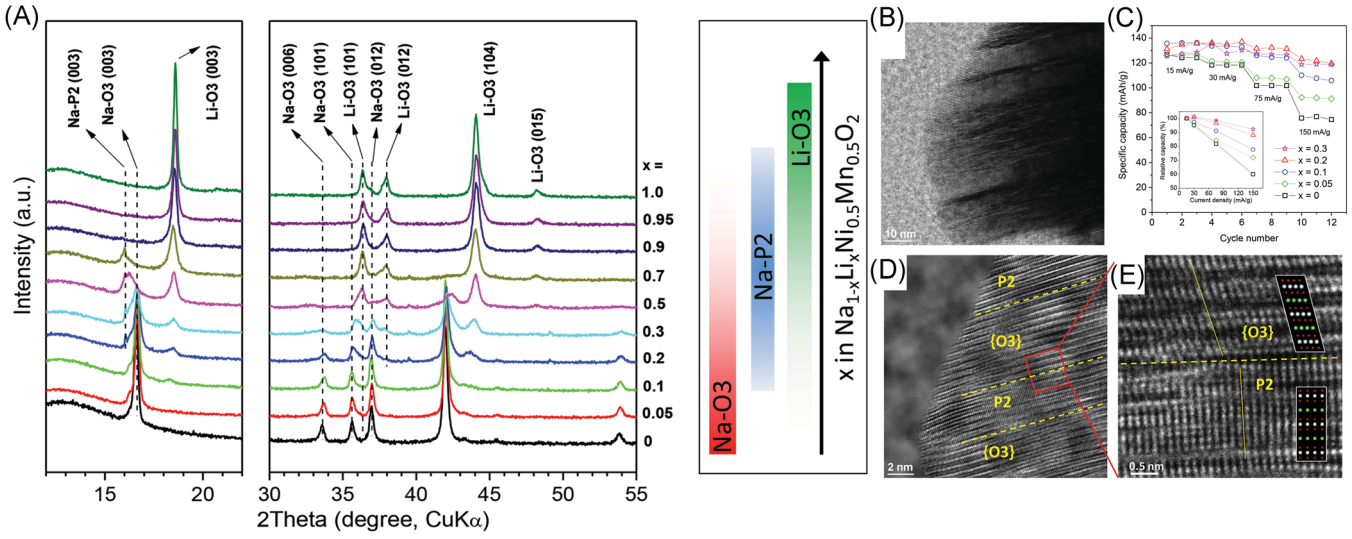

FIGURE 14 (A) X-ray diffraction of $Na_{1-x}Li_xNi_{0.5}Mn_{0.5}O_2$ indicating that the phase composition changes with Li content. (B, D, E) HR-TEM of $Na_{0.7}Li_{0.3}Ni_{0.5}Mn_{0.5}O_2$ showing atomic-level intergrowth of {Na-O3} and P2 phases. (C) Rate performance comparison for $Na_{1-x}Li_xNi_{0.5}Mn_{0.5}O_2$. Reproduced (adapted) with permission from Reference [79]. Copyright 2014, Wiley. HR-TEM, high-resolution transmission electron microscopy

reaching a maximum at $x = 0.5$. Simultaneously, the appearance of the Li-O3 phase begins at $x = 0.1$ and its phase fraction increases until the pure phase is formed at $x = 1$. The composition $Na_{0.7}Li_{0.3}Ni_{0.5}Mn_{0.5}O_2$ was further characterized by high-resolution TEM (Figure 14), revealing the atomic-level intergrowth between the {Na-O3} and P2 phases. ^{7}Li nuclear magnetic resonance (NMR) was used to study the local chemical environment of Li and indicated that Li was predominately located in the alkali layers of the various phases, with a minor component in the TM layers. Using the ionic potential of both Na and Li to determine $\bar{\Phi}_{Na}$ and from the end member ($x = 0,1$) O3 structures, some combination of Na-O3 and Li-O3 phases could reasonably be expected for this system. The appearance of the P2 phase is anomalous in material with 1:1 ratio of alkali ions to TMs, indicating the unusual effect that Li incorporation may have on the {Na-O3} structure. This was speculated to possibly arise from the heterogeneity of TM composition in the various phases, or loss of structural Na due to reaction with H_2O or CO_2. The electrochemical properties of the materials with $0 \leq x \leq 0.3$ were compared. The lithium doped samples demonstrated both increased capacity and smoother voltage profiles compared to the undoped material, suggesting that phase transition and Na/vacancy ordering processes were disrupted by Li addition. Coulombic efficiency in excess of 100% was obtained for $x \geq 0.1$ as a result of the partially Na vacant O′3 and P3 phases which could be filled after the first cycle against Na metal. Li substituted samples showed notably enhanced rate performance, with $Na_{0.7}Li_{0.3}Ni_{0.5}Mn_{0.5}O_2$ still delivering 95% of its capacity at 15 mA/g when discharged at 150 mA/g compared to only 60% for the undoped sample (Figure 14). The structural evolution of the $Na_{0.7}Li_{0.3}Ni_{0.5}Mn_{0.5}O_2$ material was studied by operando XRD and found that the P2 material experienced only <2% volume change and no phase transition when charged to 4 V. The {Na-O3} was consolidated into a single P3 phase during charge to 3.2 V that distorted to O″3 above 4 V. However, the P3 phase was recovered on discharge and persisted to the lower cutoff voltage of 2 V. The P2/P3 intergrowth structure that formed in the first cycle is able to avoid the O′3 and O3 phase regions experienced by the undoped material, which secures the fast diffusion kinetics of the prismatic Na layers. The presence of the P2 phase can stabilize the P3 structure, probably as a result of strain associated with change in lattice parameter and crystal symmetry at the phase interface. This study demonstrates the value of Li as a dopant to generate phase intergrowth, which can modify the phase transition behavior and subsequently enhance the electrochemical properties. The use of element-specific ^{7}Li NMR provides useful insight into where the dopant element is located in the structures. High spatial resolution techniques such as HAADF-STEM with EDS/EELS and/or APT could be valuable to understand how Li is distributed and how it influences the distribution of other elements in the various phases, both in this study and other similar systems.

Xiong et al. also utilized lithium doping to generate phase intergrowth from O3-$Na_{0.87}Ni_{0.4}Fe_{0.2}Mn_{0.4}O_2$ (NFM) to make O3/Spinel-$Li_{0.25}Na_{0.87}Ni_{0.4}Fe_{0.2}Mn_{0.4}O_{2+\delta}$ (LSNFM).[58] LSNFM has a total alkali content greater than one, in contrast to the previous work. Consequently, there is some uncertainty in the cation/oxygen ratio and the value of δ depends how this additional positive charge is compensated. Other than charge compensation through change of TM oxidation state, the composition designed with excess alkali content could then promote compositional or structural heterogeneity to compensate for the additional positive charge. HR-TEM revealed the intimate interface of the O3 and spinel structures (Figure 15). LSNFM was examined by both hard and soft XAS to compare the oxidation states of the TMs between the surface and bulk. Hard XAS indicated that the Ni^{2+}, Fe^{3+}, and Mn^{4+} were predominant in the bulk. In contrast to the bulk, soft XAS indicated that Mn was partially reduced at the surface, which might be related to the excess alkali content. Compared to the undoped material, LSNFM had improved discharge capacity and capacity retention, and enhanced rate performance. The enhanced rate performance likely arose from the higher Na^+ diffusion coefficient measured by galvanostatic intermittent titration technique, possibly due to the contribution of the spinel phase to Na^+ transport. The ratio of (Na+Li)/TM as well as the Na/Li ratio are clearly valuable parameters for the synthesis of intergrown mixed-phase positive electrodes.

Aside from Li, other non-TM dopants can result in intergrowth. Li and coworkers demonstrated that substitution of manganese for tin in the P2-$Na_{0.67}Ni_{0.33}Mn_{0.67-x}Sn_xO_2$ and observed the formation of P2/O3 intergrowths with increasing fraction of the O3 phase as more Sn is introduced.[99] A post-transition metal, Sn^{4+} has [Kr]$4d^{10}$ electron configuration compared to the smaller Mn^{4+} with partially filled [Ar]$3d^3$ configuration. As a consequence of the lower ionic potential of Sn^{4+}, the tendency to form O3 might be predictable. However, the O3 phase is not favorable on the basis of the cationic potential until approximately $x = 0.39$, whereas in this study at only $x = 0.2$ there was 69% phase fraction of O3. This strong deviation from expectation may arise from the distinctly different properties of Sn from Mn. The sample with near equal proportion of P2/O3 had the best performance with composition $Na_{0.67}Ni_{0.33}Mn_{0.57}Sn_{0.1}O_2$. The Sn

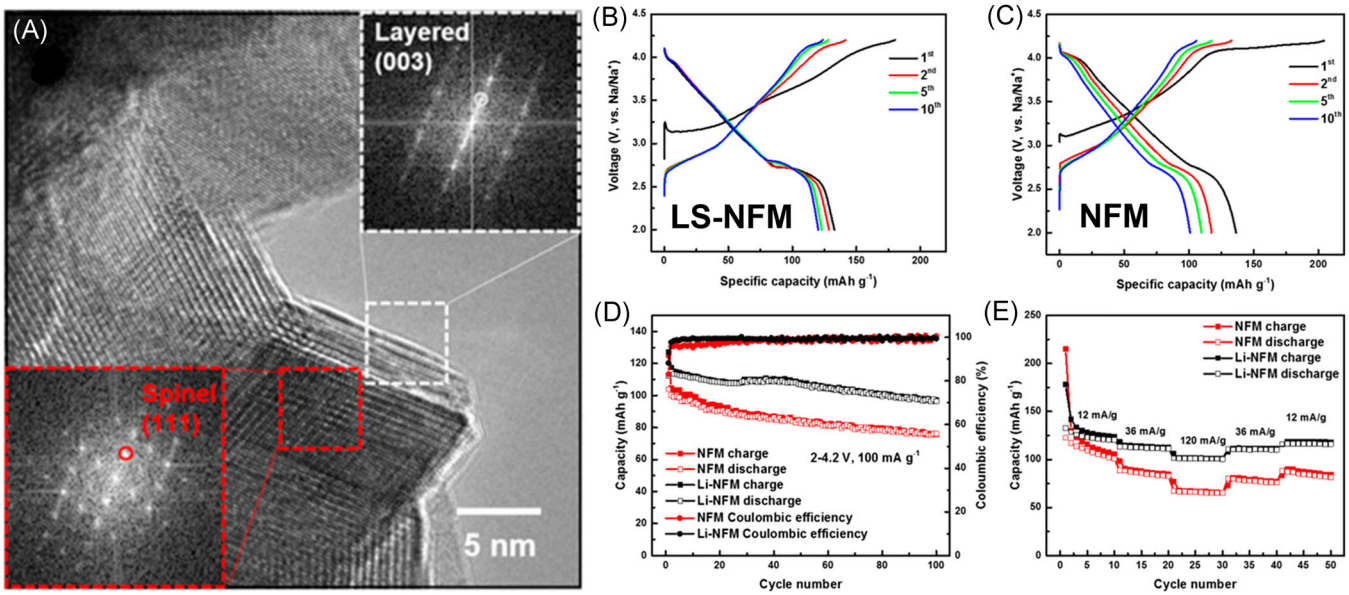

FIGURE 15 (A) HR-TEM image of O3/Spinel-$Li_{0.25}Na_{0.87}Ni_{0.4}Fe_{0.2}Mn_{0.4}O_{2+\delta}$ with inset Fourier transforms. (B, C) Voltage profiles of LSNFM and NFM for cycles 1, 2, 5, and 10. (D) Cycle life comparison. (E) Rate performance comparison. Reprinted (adapted) with permission from Reference [58]. Copyright 2018, American Chemical Society. HR-TEM, high-resolution transmission electron microscopy; LSNFM, $Li_{0.25}Na_{0.87}Ni_{0.4}Fe_{0.2}Mn_{0.4}O_{2+\delta}$; NFM, $Na_{0.87}Ni_{0.4}Fe_{0.2}Mn_{0.4}O_2$

substituted samples notably had smaller and reduced particle size, which may also significantly impact the performance. Similarly, Liang and coworkers prepared antimony substituted P2-$Na_{0.67-x}Ni_{0.33}Mn_{0.67-x}Sb_xO_2$ and observed the intergrowth of P2/O3 phases in 69/31% ratio with only $x = 0.05$.[100] Antimony is a metalloid directly neighboring Sn on the periodic table isoelectronic to Sn^{4+} as Sb^{5+} or Sn^{3+} as Sb^{2+}. As a result of the similar electronic configurations, it is unsurprising to see the elemental substitution with antimony yields similar structural behavior. In the P2/P3/spinel-$Na_{0.5}Ni_{0.2}Co_{0.15}Mn_{0.65}O_2$ and $Na_{0.5}Ni_{0.1}Co_{0.15}Mn_{0.65}Mg_{0.1}O_2$ materials, Mg^{2+} substitution for Ni^{2+} was able to regulate the phase fractions.[150] Mg substitution decreased the fraction of layered phases (P2 and P3) and increase the spinel content, which benefited the performance of the material. Clearly, the use of elements other than transition metals can result in intergrowth formation in a manner dependent on the nature of the dopant elements that may differ significantly from the TMs.

Processing efffects on phase intergrowth. Xu and coworkers utilized a strategy of controlled calcination procedure to tune the intergrowth of several phases in $NaNi_{1/3}Mn_{1/3}Co_{1/3}O_2$.[84] Dependent on the temperature and cooling procedure, biphasic P2/P3, biphasic P2/O3, or triphasic P2/O3/O1 could be formed. Utilizing in situ XRD while the calcination process progressed through heating and cooling, the structural evolution of the material was captured (Figure 16). From the structure of the precalcined (500°C for 6 h) precursor, the formation of O1 and O3 phases was evident at 655°C. At 1000°C, the triphasic P2/O3/O1 structure was clear. Then, while cooling the O3 and O1 phases disappeared at 364°C leaving only a P2/P3 biphase structure. Armed with the knowledge of the phase evolution during calcination, samples were prepared with predominately P phases (NCM-600), P2/O3 (NCM-WQ), and P2/O3/O1 (NCM-Q) by controlling the calcination temperature and quenching procedure. NCM-600 was heated at 600°C for 10 h and cooled naturally. NCM-WQ was prepared by heating to 850°C for 10 h with natural cooling, and NCM-Q was the same but with quenching at 300°C. The resulting multiphase structures were observed by XRD and had comparable phase combinations to the in situ experiment. HRTEM and electron diffraction confirmed the existence of all three phases in the NCM-Q material. The electrochemical performance of triphasic NCM-Q was superior to the biphasic NCM-WQ and P-type NCM-600, which was supported by the fully reversible structural evolution during the first charge/discharge cycle between 2 and 4.4 V. In contrast, NCM-WQ and NCM-600 had less reversible structural evolution. To evaluate the hypothesis that the triphasic intergrowth reduced the microstrain associated with charge/discharge, a Williamson-Hall analysis was performed on the in situ heating data (Figure 16). The Williamson–Hall analysis

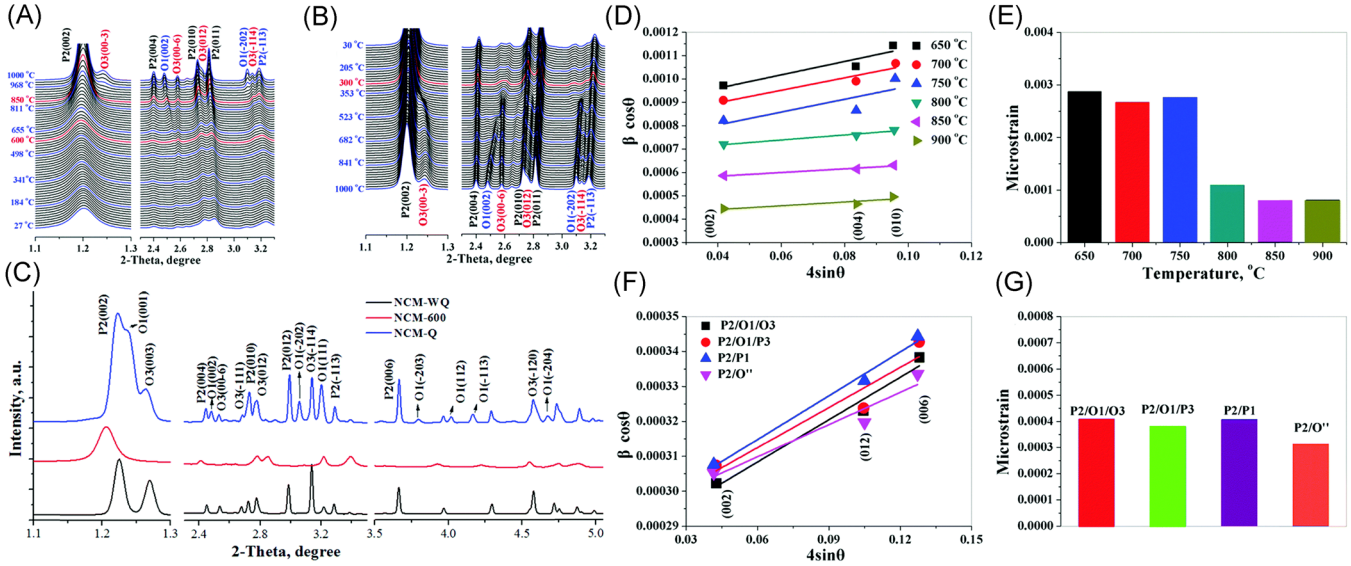

FIGURE 16 (A, B) In situ XRD of $Na_xNi_{1/3}Mn_{1/3}Co_{1/3}O_2$ during heating and cooling, respectively. (C) XRD indicating multiphasic structures resulting from different calcination procedures. (D, E) Williamson–Hall microstrain analysis of the in situ heating XRD at different temperatures, and for (F, G) NCM-Q during the first charge to 4.4 V. Reproduced (adapted) with permission from Reference [84]. Copyright 2017, Royal Society of Chemistry. XRD, X-ray diffraction

extracts information about microstrain based on the unique dependence of the peak broadening (β) on the scattering angle (θ). It was found that at higher temperatures, the microstrain could be reduced by calcination at 850–900°C. Analysis of the operando XRD of NCM-Q during charging showed that microstrain was relatively constant up to 4.4 V, suggesting that management of microstrain could have a critical role in the electrochemical performance. Microstrain management associated with the triphasic intergrowth in NCM-Q was able to suppress P2-O2 transformation during cycling, make the O1/O3 phase transformations reversible, and improve the thermal stability of the material compared to the biphasic samples. This insight into the mechanisms that provide enhanced performance is valuable for the design of high-performance multiphase LTMOs for SIBs.

Huang and coworkers similarly demonstrated that by controlling the calcination temperature, $Na_{0.62}Mn_{0.66}Ni_{0.17}Co_{0.17}O_2$ could be controlled to form either a pure P3 phase, or P3/P2 intergrowth (Figure 17).[83] The addition of lithium ($Na_{0.62}Li_{0.18}Mn0_{.66}Ni_{0.17}Co_{0.17}O_2$) to the P2/P3 material resulted in an additional O′3 phase, forming a triphasic P2/P3/Li-O′3 intergrowth. The intergrowth was observed by HAADF-STEM and EELS, which identified that Li was concentrated in the O′3 phase, suggested by the Z-contrast and Li K-edge EELS mapping. Additionally, the distribution of Na and TM species was clearly nonuniform between the phases based on HAADF-STEM EDS mapping. The triphasic structure of $Na_{0.62}Li_{0.18}Mn0_{.66}Ni_{0.17}Co_{0.17}O_2$ was able to deliver a high capacity of 224 mAh/g at low 20 mA/g rate and high 110 mAh/g capacity at 1000 mA/g. Capacity retention of 78% after 50 cycles at 40 mA/g was attributed to the stabilization provided by the triphasic structure. This study demonstrates that intergrowths formed by a combination of both processing control and dopants can result in outstanding electrochemical properties.

Guo and coworkers prepared $Na_{0.66}Li_{0.18}Mn_{0.71}Ni_{0.21}Co_{0.08}O_{2+\delta}$ with both pure P2 and P2/O3 intergrowth structures (Figure 18).[80] The pure P2 phase was synthesized by ball-milling a mixture of transition metal acetates with sodium and lithium carbonate in alcohol, followed by conventional calcination. The precursor for the P2/O3 material was prepared by coprecipitation of the transition metal acetates with lithium hydroxide and residual lithium rinsed away. The coprecipitated precursor was mixed with sodium carbonate and lithium hydroxide, then calcined in the same manner as the pure P2 material. The P2/O3 composite appeared to have uniform distribution of transition metal elements and sodium from SEM-EDS mapping. However, the lithium distribution is unknown because EDS cannot easily detect Li. The biphasic material had significantly increased capacity (200 mAh/g up from 125 mAh/g) and capacity retention of 75% after 150 cycles at 50 mA/g current. The formation of the P2/O3 intergrowth structure from variation of only the precursor processing is noteworthy and suggests the importance of understanding

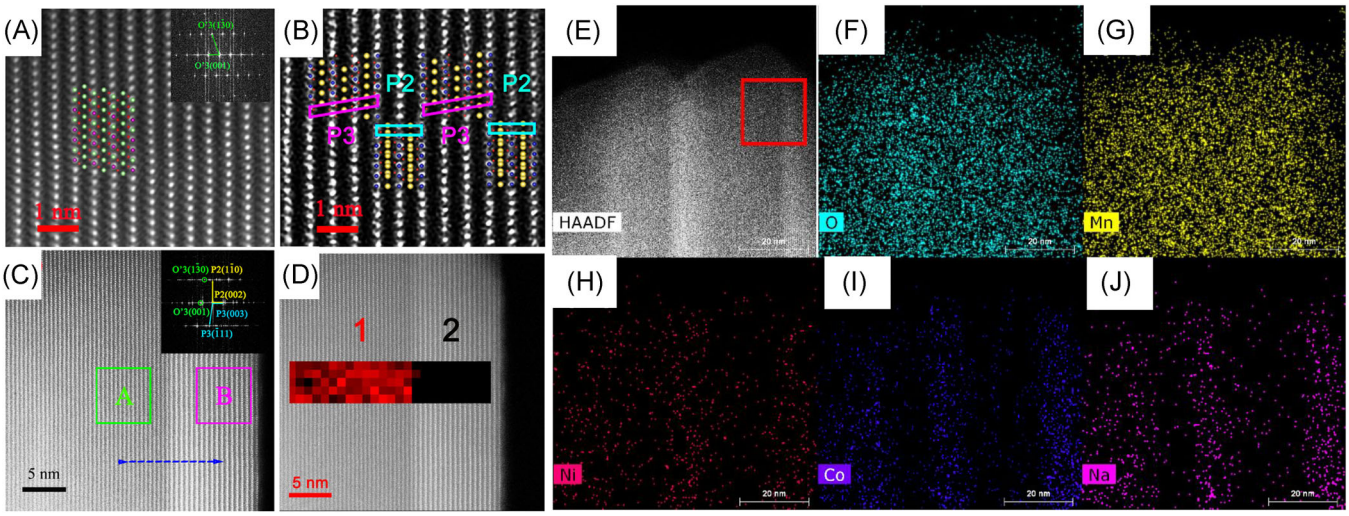

FIGURE 17 (A, B) HAADF-STEM of $Na_{0.62}Li_{0.18}Mn0_{.66}Ni_{0.17}Co_{0.17}O_2$ showing the P2, P3, and O′3 intergrowth. (C, D) EELS mapping of Li K-edge showing Li enrichment in the O′3 phase. (E–J) EDS mapping demonstrating nonuniform concentration of Na and TM between phases. Reprinted (adapted) from Reference [83] with permission. Copyright 2018, American Chemical Society. EDS, energy dispersive X-ray spectroscopy; EELS, electron energy-loss spectroscopy; HAADF-STEM, high-angle annular dark-field scanning transmission electron microscopy; TM, transition metal

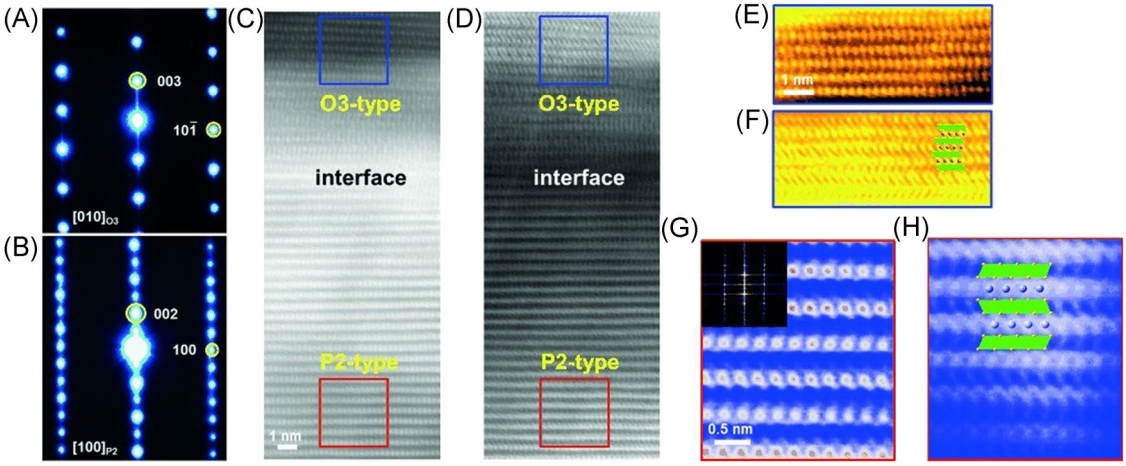

FIGURE 18 The selected-area electron diffraction patterns of P2 + O3 $Na_{0.66}Li_{0.18}Mn_{0.71}Ni_{0.21}Co_{0.08}O_{2+\delta}$: (A) O3-type structure and (B) P2-type structure. The STEM images: (C) HAADF and (D) annular bright field images of P2 + O3 NaLiMNC composite; the blue and red rectangle represent O3 structure and P2 structure areas. The enlarged images corresponding to the rectangle areas are shown in (E), (F), (G), and (H). Reproduced from Reference [80] with permission. Copyright 2015, Wiley. HAADF, high-angle annular dark-field; STEM, scanning transmission electron microscopy

the reaction pathway to generate multiphase intergrowths. The electrochemical performance may also be affected by differences in morphology or crystallinity associated with the different precursor; though it is clearly an important factor, the intergrowth may not be the sole reason for the observed performance difference.

In general, it is important to consider that variation in processing or composition will affect properties other than structure, which must be accounted for in the interpretation of altered properties and performance. To accurately determine which interactions are affecting electrochemical properties, it is essential to utilize tools that span multiple length and time scales.[153] The development of high-performance layered transition metal oxide positive electrodes for SIBs stands to benefit greatly from the ideas and methods demonstrated in the work reviewed here but still faces significant challenges.

4 | CHALLENGES FOR MULTIPHASE LTMOS

Despite the apparent opportunity to enhance the properties of LTMOs through heterogeneity of structure and composition, they still may suffer the same degradation processes as single-phase materials (air instability, phase transitions, reactions with electrolyte, etc.). Furthermore, the heterogeneity inherent to multiphase LTMOs presents additional difficulties in their design, synthesis, and characterization.

4.1 | Design

Numerous factors critically affect multiphase structure, especially composition and processing conditions. Predictive models such as the cationic potential for single phase material structure are limited in their scope, and ab initio calculations may be limited to capture the complex nature of the electronic structure of transition metals and other ions. Extending the already enormous single-phase design space to allow multiple phases greatly compounds this issue. The formation of multiphase materials from coating processes on single phase LTMOs can be intuitive, but the more complex cases of nanoscale interfaces in the bulk or spontaneous segregation of specific elements to the surface is challenging to predict. In these cases, the state of the art for design strategy is a balance of 'guess-and-check' over many compositions and processing conditions,[96] with guidance borrowed from tools to predict single phase structure (i.e., cationic potential[19]) combined with scientific intuition. Consequently, it may be highly resource and labor intensive to identify new multiphase materials with nanoscale phase interfaces. Refinement of predictive methods to directly target multiphases with specific spatial heterogeneities remains greatly needed.

4.2 | Synthesis

Spatial heterogeneities generated intentionally via advanced synthesis methods (e.g., coprecipitated core-shell precursors, ALD coatings) will necessarily add complexity, additional processing time, cost, and may require considerable optimization. This heterogeneity must also be carefully preserved during further processing where high temperature could drive diffusion, which may reduce or eliminate the designed heterogeneity. These factors must be thoughtfully balanced against the property enhancements that brought on by the modified synthesis. Additionally, in cases where metastable, multiphase LTMOs result from transient states during processing it is critical that materials are prepared with extreme attention to detail to achieve reliable results. Other than widely discussed factors such as precursor compound choice and calcination temperature, it is our experience that even slight variations during calcination in parameters such as atmosphere, gas flow rate, quenching rate, total sample mass, and so forth. can have substantial effect on the multiphase structures and relative phase fraction. The additional precision required to fully control multiphase LTMO structures demands additional caution compared to single phase materials, which may already be nontrivial to synthesize repeatably and reliably.

4.3 | Characterization

Examination of the properties of single-phase materials often makes the reasonable assumption that the properties of the pristine material do not vary significantly spatially - other than perhaps near to the surface or after electrochemical cycling, degradation due to air exposure, or other processing known to impart spatial heterogeneity. Investigation of many distinct particles in *pristine* single-phase materials then primarily serves to establish the degree of variance from the secondary particle scale to the electrode scale. This gives some degree of confidence that few repeated measurements will give results representative of the sample as a whole. In contrast, no such assumptions should be made without significant prior evidence for pristine multiphase materials. Multiphase materials must be investigated with spatially resolved techniques that can identify differences at a length scale smaller than primary particles, up to the secondary particle and electrode scale to establish the exact nature of the heterogeneity. Without such investigation, it cannot be known if the multiphase material is a macroscopic or microscopic mixture, or a nanoscale integration of the phases. This information is critical to the accurate interpretation of phase change behavior, reaction with electrolyte or air, and other degradation mechanisms that can further modify the spatial distribution of properties. The higher standard of spatially resolved characterization makes the study of multiphase LTMOs significantly more challenging than single-phase materials, which are already highly complex. The application of computational methods to investigate the mechanisms of property change in multiphase LTMOs may also be hindered if accurate information about both local and long-range structure is unavailable, or if the length scale of the phase interfaces is too large to compute practically. The accessibility of techniques with both high spatial resolution and sufficient throughput

that can establish variance attributable to a wide range of length scales is limited, typically requiring synchrotron facilities (e.g., TXM) and/or advanced microscopy instrumentation (e.g., atomic resolution HAADF-STEM with EDS/EELS). The necessity of low-availability characterization methods is a significant hinderance and slows the learning rate of multiphase LTMO development.

5 | SUMMARY AND OUTLOOK

Multiphase LTMOs for SIB positive electrodes with phase interfaces across multiple length scales are a promising avenue toward practical, high-performance SIBs. The existing work on multiphase LTMOs for SIB positive electrode materials proves that materials with high energy and power density, electrochemical and environmental stability, made from low-cost sustainable resources are fully within the realm of possibility. Phases will complement each other's strengths and mitigate their weaknesses if interfaces are carefully controlled. Multiphase materials can stabilize against phase transitions, suppress reaction with air and electrolyte, and enhance rate performance and capacity. To achieve such enhancements, all interfaces and length scales must be considered carefully because of their distinct effects on properties and performance. Informed design and synthesis strategies have been shown to effectively manipulate phase interfaces from nanometer to electrode length scales.

Phase interfaces at the micrometer scale occur at the surface and in the bulk. Coprecipitation can modify composition spatially at micrometer scale to affect ionic potential, which provides the means for controlling structure and properties within secondary particles. At the nanometer scale, surface phases can be produced via liquid-based coating technique, spontaneous surface segregation, and self-limiting coating chemistry (ALD/MLD). In the bulk of individual primary particles, nanometer-scale phase intergrowth can form due to variation of Na content, transition metal composition, doping (especially Li), and from processing effects such as temperature and cooling procedure.

To design multiphase positive electrode materials, the oxidation states of the transition metals must be carefully balanced to avoid impurities and control structural distortion while still providing high capacity for energy storage. The unique chemical properties of the transition metals and dopants, especially size and charge, in combination with the synthesis methods strongly affects the heterogeneity of phase and composition distribution. However, design strategies to intentionally develop nanoscale phase interfaces are currently underdeveloped and warrant significant further study. Additionally, the enhanced sensitivity of multiphase material properties (e.g., relative phase fractions) to the processing conditions necessitates increased process precision to achieve repeatable and reliable results, especially in the common case of transient or metastable multiphase materials.

To understand exactly how and why the heterogeneity of phases affects electrochemical properties, characterization techniques must match length scale of phase interactions. High spatial resolution combined with chemical sensitivity is critically important toward understanding phase interactions. Techniques of particular importance include X-ray and electron microscopy (e.g., TXM, XRD, TEM/STEM), associated chemically sensitive spectroscopy methods (e.g., EELS, EDS, XAS, Time-of-Flight Secondary Ion Mass Spectrometry) and surface sensitive tools (e.g., XPS, EIS, Raman, soft XAS). High spatial resolution techniques often provide only local information, so it is essential that multimodal, complementary characterizations are implemented to accurately differentiate local deviations in properties from those at longer length scales. Application of in situ and operando characterizations that allow the structure evolution during synthesis and electrochemical operation provide essential insight into how multiphase materials can be designed and reveal their mechanisms of phase transitions during cycling. However, the necessity for more advanced, but less accessible characterization techniques makes the study of multiphase LTMOs even more challenging than their single-phase counterparts.

The importance of multiphase, heterogeneous positive electrodes is apparent if high-performance SIBs are to be realized. Continued effort toward the design, synthesis, and characterization of multiphase LTMOs is of great value to society as these materials become increasingly important to enable large-scale energy storage for renewable energy sources.

ACKNOWLEDGMENTS

This material is based upon work supported by the U.S. Department of Energy, Office of Science, Office of Basic Energy Sciences program under Award Number DE-SC0019121. The work by E.L. was supported by the Advanced Battery Materials Research (BMR) Program of the U.S. Department of Energy (DOE), Office of Energy Efficiency and Renewable Energy.

ORCID

Eric Gabriel http://orcid.org/0000-0002-1026-2413

REFERENCES

1. Liu Q, Hu Z, Chen M, et al. The cathode choice for commercialization of sodium-ion batteries: layered transition metal oxides versus prussian blue analogs. *Adv Funct Mater*. 2020;30(14):1909530. https://doi.org/10.1002/adfm.201909530
2. Tian Y, Zeng G, Rutt A, et al. Promises and challenges of next-generation "beyond Li-ion" batteries for electric vehicles and grid decarbonization. *Chem Rev*. 2021;121(3):1623-1669. https://doi.org/10.1021/acs.chemrev.0c00767
3. FCAB. National Blueprint for Lithium Batteries 2021–2030.
4. Haynes WM. *CRC Handbook of Chemistry and Physics*. CRC Press; 2016.
5. Yabuuchi N, Yoshida H, Komaba S. Crystal structures and electrode performance of Alpha-$NaFeO_2$ for rechargeable sodium batteries. *Electrochemistry*. 2012;80(10):716-719.
6. Liu Q, Hu Z, Li W, et al. Sodium transition metal oxides: the preferred cathode choice for future sodium-ion batteries? *Energy Env Sci*. 2021;14(1):158-179. https://doi.org/10.1039/D0EE02997A
7. Yabuuchi N, Kubota K, Dahbi M, Komaba S. Research development on sodium-ion batteries. *Chem Rev*. 2014;114(23):11636-11682. https://doi.org/10.1021/cr500192f
8. Kubota K, Dahbi M, Hosaka T, Kumakura S, Komaba S. Towards K-ion and Na-ion batteries as "beyond Li-ion". *Chem Rec*. 2018;18(4):459-479. https://doi.org/10.1002/tcr.201700057
9. Vaalma C, Buchholz D, Weil M, Passerini S. A cost and resource analysis of sodium-ion. *Batteries Nat Rev Mater*. 2018;3:18013.
10. Delmas C, Carlier D, Guignard M. The layered oxides in lithium and sodium-ion batteries: a solid-state chemistry approach. *Adv Energy Mater*. 2021;11(2):2001201. https://doi.org/10.1002/aenm.202001201
11. Gao R-M, Zheng Z-J, Wang P-F, Wang C-Y, Ye H, Cao F-F. Recent advances and prospects of layered transition metal oxide cathodes for sodium-ion batteries. *Energy Storage Mater*. 2020;30:9-26. https://doi.org/10.1016/j.ensm.2020.04.040
12. Liu Q, Hu Z, Chen M, et al. Recent progress of layered transition metal oxide cathodes for sodium-ion batteries. *Small*. 2019;15(32):1805381. https://doi.org/10.1002/smll.201805381
13. Wang P, You Y, Yin Y, Guo Y. Layered oxide cathodes for sodium-ion batteries: phase transition, air stability, and performance. *Adv Energy Mater*. 2018;8(8):1701912.
14. Wang S, Sun C, Wang N, Zhang Q. Ni- and/or Mn-based layered transition metal oxides as cathode materials for sodium ion batteries: status, challenges and countermeasures. *J Mater Chem A*. 2019;7(17):10138-10158. https://doi.org/10.1039/C8TA12441H
15. Su H, Jaffer S, Yu H. Transition metal oxides for sodium-ion batteries. *Energy Storage Mater*. 2016;5:116-131. https://doi.org/10.1016/j.ensm.2016.06.005
16. Stansby JH, Sharma N, Goonetilleke D. Probing the charged state of layered positive electrodes in sodium-ion batteries: reaction pathways, stability and opportunities. *J Mater Chem A*. 2020;8(47):24833-24867. https://doi.org/10.1039/D0TA09553B
17. Delmas C, Fouassier C, Hagenmuller P. Structural classification and properties of the layered oxides. *Phys. BC*. 1980;99(1):81-85. https://doi.org/10.1016/0378-4363(80)90214-4
18. Han MH, Gonzalo E, Casas-Cabanas M, Rojo T. Structural evolution and electrochemistry of monoclinic $NaNiO_2$ upon the first cycling process. *J Power Sources*. 2014;258:266-271. https://doi.org/10.1016/j.jpowsour.2014.02.048
19. Zhao C, Wang Q, Yao Z, et al. Rational design of layered oxide materials for sodium-ion batteries. *Science*. 2020;370(6517):708-711. https://doi.org/10.1126/science.aay9972
20. Lei Y, Li X, Liu L, Ceder G. Synthesis and stoichiometry of different layered sodium cobalt oxides. *Chem Mater*. 2014;26(18):5288-5296. https://doi.org/10.1021/cm5021788
21. Lu Z, Donaberger RA, Dahn JR. Superlattice ordering of Mn, Ni, and Co in layered alkali transition metal oxides with P2, P3, and O3 structures. *Chem Mater*. 2000;12(12):3583-3590. https://doi.org/10.1021/cm000359m
22. Guo S, Li Q, Liu P, Chen M, Zhou H. Environmentally stable interface of layered oxide cathodes for sodium-ion batteries. *Nat Commun*. 2017;8(1):135. https://doi.org/10.1038/s41467-017-00157-8
23. Sato T, Sato K, Zhao W, Kajiya Y, Yabuuchi N. Metastable and nanosize cation-disordered rocksalt-type oxides: revisit of stoichiometric $LiMnO_2$ and $NaMnO_2$. *J Mater Chem A*. 2018;6(28):13943-13951. https://doi.org/10.1039/C8TA03667E
24. Bianchini M, Wang J, Clément RJ, et al. The interplay between thermodynamics and kinetics in the solid-state synthesis of layered oxides. *Nat Mater*. 2020;19(10):1088-1095. https://doi.org/10.1038/s41563-020-0688-6
25. Komaba S, Yabuuchi N, Nakayama T, Ogata A, Ishikawa T, Nakai I. Study on the reversible electrode reaction of $Na_{1-X}Ni_{0.5}Mn_{0.5}O_2$ for a rechargeable sodium-ion battery. *Inorg Chem*. 2012;51(11):6211-6220. https://doi.org/10.1021/ic300357d
26. Lu Z, Dahn J. In situ X-ray diffraction study of P2 $Na_{2/3}$ $[Ni_{1/3}Mn_{2/3}]$ O_2. *J Electrochem Soc*. 2001;148(11):A1225-A1229.
27. Fielden R, Obrovac M. Investigation of the $NaNi_xMn_{1-X}O_2$ ($0\leq X\leq 1$) system for Na-ion battery cathode materials. *J Electrochem Soc*. 2015;162(3):A453-A459.
28. Yu H, Guo S, Zhu Y, Ishida M, Zhou H. Novel titanium-based O_3-type $NaTi_{0.5}Ni_{0.5}O_2$ as a cathode material for sodium ion batteries. *Chem Commun*. 2014;50(4):457-459.
29. Yoshida H, Yabuuchi N, Komaba S. $NaFe_{0.5}Co_{0.5}O_2$ as high energy and power positive electrode for Na-ion batteries. *Electrochem Commun*. 2013;34:60-63.
30. Sathiya M, Hemalatha K, Ramesha K, Tarascon J-M, Prakash AS. Synthesis, structure, and electrochemical properties of the layered sodium insertion cathode material: $NaNi_{1/3}Mn_{1/3}Co_{1/3}O_2$. *Chem Mater*. 2012;24(10):1846-1853. https://doi.org/10.1021/cm300466b
31. Vassilaras P, Toumar AJ, Ceder G. Electrochemical properties of $NaNi_{1/3}Co_{1/3}Fe_{1/3}O_2$ as a cathode material for Na-ion batteries. *Electrochem Commun*. 2014;38:79-81.
32. Kim D, Lee E, Slater M, Lu W, Rood S, Johnson CS. Layered $Na[Ni_{1/3}Fe_{1/3}Mn_{1/3}]O_2$ cathodes for Na-ion battery application. *Electrochem Commun*. 2012;18:66-69.
33. Li Y, Gao Y, Wang X, et al. Iron Migration and oxygen oxidation during sodium extraction from $NaFeO_2$. *Nano Energy*. 2018;47:519-526. https://doi.org/10.1016/j.nanoen.2018.03.007
34. Yu T-Y, Kim J, Hwang J-Y, et al. High-energy O_3-$Na_{1-2x}Ca_x[Ni_{0.5}Mn_{0.5}]O_2$ cathodes for long-life sodium-ion

batteries. *J Mater Chem A*. 2020;8(27):13776-13786. https://doi.org/10.1039/D0TA04847J

35. Kubota K, Fujitani N, Yoda Y, Kuroki K, Tokita Y, Komaba S. Impact of Mg and Ti doping in O3 type $NaNi_{1/2}Mn_{1/2}O_2$ on reversibility and phase transition during electrochemical Na intercalation. *J Mater Chem A*. 2021;9(21):12830-12844. https://doi.org/10.1039/D1TA01164B
36. Susanto D, Cho MK, Ali G, et al. Anionic redox activity as a key factor in the performance degradation of $NaFeO_2$ cathodes for sodium ion batteries. *Chem Mater*. 2019;31(10):3644-3651. https://doi.org/10.1021/acs.chemmater.9b00149
37. Yabuuchi N, Kajiyama M, Iwatate J, et al. P2-type $Na_x[Fe_{1/2}Mn_{1/2}]O_2$ made from earth-abundant elements for rechargeable Na Bbatteries. *Nat Mater*. 2012;11(6):512-517.
38. Clément RJ, Bruce PG, Grey CP. Manganese-based P2-type transition metal oxides as sodium-ion battery cathode materials. *J Electrochem Soc*. 2015;162(14):A2589-A2604.
39. Risthaus T, Zhou D, Cao X, et al. A high-capacity P2 $Na_2/3Ni_{1/3}Mn_2/3O_2$ cathode material for sodium ion batteries with oxygen activity. *J Power Sources*. 2018;395:16-24.
40. Wang H, Yang B, Liao X-Z, et al. Electrochemical properties of P2-$Na_{2/3}$ $[Ni_{1/3}Mn_{2/3}]$ O_2 cathode material for sodium ion batteries when cycled in different voltage ranges. *Electrochim Acta*. 2013;113:200-204.
41. Yang Q, Wang P-F, Guo J-Z, et al. Advanced P2-$Na_2/3Ni_1/3Mn_7/12Fe_1/12O_2$ cathode material with suppressed P2–O2 phase transition toward high-performance sodium-ion battery. *ACS Appl Mater Interfaces*. 2018;10(40):34272-34282.
42. Zhao W, Tanaka A, Momosaki K, et al. Enhanced electrochemical performance of Ti substituted P2-$Na_2/3Ni_1/4Mn_3/4O_2$ cathode material for sodium ion batteries. *Electrochim Acta*. 2015;170:171-181. https://doi.org/10.1016/j.electacta.2015.04.125
43. Zhao J, Xu J, Lee DH, Dimov N, Meng YS, Okada S. Electrochemical and thermal properties of P2-type $Na_2/3Fe_1/3Mn_2/3O_2$ for Na-ion batteries. *J Power Sources*. 2014;264:235-239.
44. Zheng L, Li J, Obrovac MN. Crystal structures and electrochemical performance of air-stable $Na_2/3Ni_1/3$–XCux$Mn_2/3O_2$ in sodium cells. *Chem Mater*. 2017;29(4):1623-1631. https://doi.org/10.1021/acs.chemmater.6b04769
45. Risthaus T, Chen L, Wang J, et al. P3 $Na_{0.9}Ni_{0.5}Mn_{0.5}O_2$ cathode material for sodium ion batteries. *Chem Mater*. 2019;31(15):5376-5383.
46. Kalapsazova M, Ortiz GF, Tirado JL, et al. P3-Type layered sodium-deficient nickel–manganese oxides: a flexible structural matrix for reversible sodium and lithium intercalation. *ChemPlusChem*. 2015;80(11):1642-1656.
47. Zhou Y-N, Wang P-F, Zhang X-D, et al. Air-stable and high-voltage layered P3-type cathode for sodium-ion full battery. *ACS Appl Mater Interfaces*. 2019;11(27):24184-24191.
48. Kim D, Kang S, Slater M, et al. Enabling sodium batteries using lithium-substituted sodium layered transition metal oxide cathodes. *Adv Energy Mater*. 2011;1(3):333-336.
49. Kubota K, Komaba S. Review—practical issues and future perspective for Na-ion batteries. *J Electrochem Soc*. 2015;162(14):A2538-A2550. https://doi.org/10.1149/2.0151514jes
50. Deng J, Luo W-B, Chou S-L, Liu H-K, Dou S-X. Sodium-ion batteries: from academic research to practical commercialization. *Adv Energy Mater*. 2018;8(4):1701428. https://doi.org/10.1002/aenm.201701428
51. Duffort V, Talaie E, Black R, Nazar LF. Uptake of CO_2 in layered P2-$Na_{0.6}7Mn_{0.5}Fe_{0.5}O_2$: insertion of carbonate anions. *Chem Mater*. 2015;27:2515-2524.
52. Zheng L, Li L, Shunmugasundaram R, Obrovac MN. Effect of controlled-atmosphere storage and ethanol rinsing on $NaNi_{0.5}Mn_{0.5}O_2$ for sodium-ion batteries. *ACS Appl Mater Interfaces*. 2018;10(44):38246-38254.
53. Lu Z, Dahn JR. Intercalation of water in P2, T2 and O2 structure $Az[CO_xNi_{1/3-X}Mn_{2/3}]O_2$. *Chem Mater*. 2001;13:1252-1257.
54. Mariyappan S, Wang Q, Tarascon JM. Will sodium layered oxides ever be competitive for sodium ion battery applications? *J Electrochem Soc*. 2018;165(16):A3714-A3722.
55. Yabuuchi N, Yano M, Yoshida H, Kuze S, Komaba S. Synthesis and electrode performance of O3-type $NaFeO_2$-$NaNi_{1/2}Mn_{1/2}O_2$ solid solution for rechargeable sodium batteries. *J Electrochem Soc*. 2013;160(5):A3131-A3137.
56. Yuan DD, Wang YX, Cao YL, Ai XP, Yang HX. Improved electrochemical performance of Fe-substituted $NaNi_{0.5}Mn_{0.5}O_2$ cathode materials for sodium-ion batteries. *ACS Appl Mater Interfaces*. 2015;7(16):8585-8591. https://doi.org/10.1021/acsami.5b00594
57. Sun L, Xie Y, Liao X, et al. Insight into Ca-substitution effects on O3-type $NaNi_{1/3}Fe_{1/3}Mn_{1/3}O_2$ cathode materials for sodium-ion batteries application. *Small*. 2018;14(21):1704523.
58. Deng C, Skinner P, Liu Y, et al. Li-substituted layered spinel cathode material for sodium ion batteries. *Chem Mater*. 2018;30(22):8145-8154. https://doi.org/10.1021/acs.chemmater.8b02614
59. Wang P, Yao H, Liu X, et al. Ti-substituted $NaNi_{0.5}Mn_{0.5-x}Ti_xO_2$ cathodes with reversible O3−P3 phase transition for high-performance sodium-ion batteries. *Adv Mater*. 2017;29(19):1700210.
60. Park J, Park G, Kwak HH, Hong S-T, Lee J. Enhanced rate capability and cycle performance of titanium-substituted P2-type $Na_{0.67}Fe_{0.5}Mn_{0.5}O_2$ as a cathode for sodium-ion batteries. *ACS Omega*. 2018;3(1):361-368. https://doi.org/10.1021/acsomega.7b01481
61. Wang Y, Wang L, Zhu H, et al. Ultralow-strain Zn-substituted layered oxide cathode with suppressed P2–O2 transition for stable sodium ion storage. *Adv Funct Mater*. 2020;30(13):1910327. https://doi.org/10.1002/adfm.201910327
62. Zhou C, Yang L, Zhou C, et al. Co-Substitution enhances the rate capability and stabilizes the cyclic performance of O3-type cathode $NaNi_{0.45-X}Mn_{0.25}Ti_{0.3}Co_xO_2$ for sodium-ion storage at high voltage. *ACS Appl Mater Interfaces*. 2019;11(8):7906-7913. https://doi.org/10.1021/acsami.8b17945
63. Wang L, Sun Y-G, Hu L-L, et al. Copper-substituted $Na_{0.67}Ni_{0.3-x}Cu_xMn_{0.7}O_2$ cathode materials for sodium-ion batteries with suppressed P2–O2 phase transition. *J Mater Chem A*. 2017;5(18):8752-8761.
64. Ponrouch A, Monti D, Boschin A, Steen B, Johansson P, Palacín MR. Non-aqueous electrolytes for sodium-ion batteries. *J Mater Chem A*. 2015;3(1):22-42. https://doi.org/10.1039/C4TA04428B
65. Ponrouch A, Dedryvère R, Monti D, et al. Towards high energy density sodium ion batteries through electrolyte

optimization. *Energy Env. Sci*. 2013;6(8):2361-2369. https://doi.org/10.1039/C3EE41379A

66. Huang Y, Zhao L, Li L, Xie M, Wu F, Chen R. Electrolytes and electrolyte/electrode interfaces in sodium-ion batteries: from scientific research to practical application. *Adv Mater*. 2019;31(21):1808393.
67. Li P, Kim H, Myung S-T, Sun Y-K. Diverting exploration of silicon anode into practical way: a review focused on silicon-graphite composite for lithium ion batteries. *Energy Storage Mater*. 2021;35:550-576. https://doi.org/10.1016/j.ensm.2020.11.028
68. Zielke L, Sun F, Markötter H, et al. Synchrotron X-ray tomographic study of a silicon electrode before and after discharge and the effect of cavities on particle fracturing. *ChemElectroChem*. 2016;3(7):1170-1177.
69. Wu J, Zhu Z, Zhang H, et al. Improved electrochemical performance of the silicon/graphite-tin composite anode material by modifying the surface morphology of the Cu current collector. *Electrochim Acta*. 2014;146:322-327.
70. Ramasamy HV, Didwal PN, Sinha S, et al. Atomic layer deposition of Al_2O_3 on P2-$Na_{0.5}Mn_{0.5}Co_{0.5}O_2$ as interfacial layer for high power sodium-ion batteries. *J Colloid Interface Sci*. 2020;564:467-477.
71. Chu S, Jia X, Wang J, et al. Reduced air sensitivity and improved electrochemical stability of P2–$Na_2/3Mn_1/2Fe_1/4Co_1/4O_2$ through atomic layer deposition-assisted Al_2O_3 coating. *Compos Part B Eng*. 2019;173:106913.
72. Alvarado J, Ma C, Wang S, Nguyen K, Kodur M, Meng YS. Improvement of the cathode electrolyte interphase on P2-$Na_2/3Ni_{1/3}Mn_{2/3}O_2$ by atomic layer deposition. *ACS Appl Mater Interfaces*. 2017;9(31):26518-26530.
73. Liu Y, Fang X, Zhang A, et al. Layered P2-$Na_{2/3}[Ni_{1/3}Mn_{2/3}]O_2$ as high-voltage cathode for sodium-ion batteries: the capacity decay mechanism and Al_2O_3 surface modification. *Nano Energy*. 2016;27:27-34.
74. Hwang J-Y, Yu T-Y, Sun Y-K. Simultaneous MgO coating and Mg doping of $Na[Ni_{0.5}Mn_{0.5}]O_2$ cathode: facile and customizable approach to high-voltage sodium-ion batteries. *J Mater Chem A*. 2018;6(35):16854-16862.
75. Chen C, Han Z, Chen S, et al. Core–shell layered oxide cathode for high-performance sodium-ion batteries. *ACS Appl Mater Interfaces*. 2020;12(6):7144-7152. https://doi.org/10.1021/acsami.9b19260
76. Hou P, Zhang H, Zi Z, Zhang L, Xu X. Core–shell and concentration-gradient cathodes prepared via co-precipitation reaction for advanced lithium-ion batteries. *J Mater Chem A*. 2017;5(9):4254-4279.
77. Kim D, Sandi G, Croy JR, et al. Composite 'layered-layered-spinel' cathode structures for lithium-ion batteries. *J Electrochem Soc*. 2012;160(1):A31-A38. https://doi.org/10.1149/2.049301jes
78. Long BR, Croy JR, Park JS, Wen J, Miller DJ, Thackeray MM. Advances in stabilizing 'layered-layered' $XLi_2MnO3\cdot(1-x)LiMO_2$ (M= Mn, Ni, Co) electrodes with a spinel component. *J Electrochem Soc*. 2014;161(14):A2160-A2167.
79. Lee E, Lu J, Ren Y, et al. Layered P2/O3 intergrowth cathode: toward high power Na-ion batteries. *Adv Energy Mater*. 2014;4(17):1400458. https://doi.org/10.1002/aenm.201400458
80. Guo S, Liu P, Yu H, et al. A layered P2- and O3-type composite as a high-energy cathode for rechargeable sodium-ion batteries. *Angew Chem Int Ed*. 2015;54(20):5894-5899. https://doi.org/10.1002/anie.201411788
81. Qi X, Liu L, Song N, et al. Design and comparative study of O3/P2 hybrid structures for room temperature sodium-ion batteries. *ACS Appl Mater Interfaces*. 2017;9(46):40215-40223.
82. Chen J, Li L, Wu L, et al. Enhanced cycle stability of $Na_{0.9}Ni_{0.45}Mn_{0.55}O_2$ through tailoring O3/P2 hybrid structures for sodium-ion batteries. *J Power Sources*. 2018;406:110-117.
83. Huang Q, Xu S, Xiao L, et al. Improving the electrochemical properties of the manganese-based P3 phase by multiphasic intergrowth. *Inorg Chem*. 2018;57(24):15584-15591. https://doi.org/10.1021/acs.inorgchem.8b02931
84. Xu G-L, Amine R, Xu Y-F, et al. Insights into the structural effects of layered cathode materials for high voltage sodium-ion batteries. *Energy Environ Sci*. 2017;10(7):1677-1693.
85. Rahman MM, Xu Y, Cheng H, et al. Empowering multi-component cathode materials for sodium ion batteries by exploring three-dimensional compositional heterogeneities. *Energy Environ Sci*. 2018;11(9):2496-2508.
86. Deng Q, Zheng F, Zhong W, et al. Nanoscale surface modification of P2-type $Na_{0.65}[Mn_{0.70}Ni_{0.16}Co_{0.14}]O_2$ cathode material for high-performance sodium-ion batteries. *Chem Eng J*. 2021;404:126446. https://doi.org/10.1016/j.cej.2020.126446.
87. Jo C-H, Jo J-H, Yashiro H, Kim S-J, Sun Y-K, Myung S-T. Bioinspired surface layer for the cathode material of high-energy-density sodium-ion batteries. *Adv Energy Mater*. 2018;8(13):1702942. https://doi.org/10.1002/aenm.201702942
88. Kim H, Park J-H, Kim S-C, et al. Multiple effects of $Mg_{1-X}Ni_xO$ coating on P2-Type $Na_{0.67}Ni_{0.33}Mn_{0.67}O_2$ to generate highly stable cathodes for sodium-ion batteries. *J Alloys Compd*. 2021;856:157294. https://doi.org/10.1016/j.jallcom.2020.157294
89. Zhang Y, Pei Y, Liu W, et al. $AlPO_4$-coated P2-type hexagonal $Na_{0.7}MnO_{2.05}$ as high stability cathode for sodium ion battery. *Chem Eng J*. 2020;382:122697. https://doi.org/10.1016/j.cej.2019.122697
90. Li W, Yao Z, Zhang S, et al. Building superior layered oxide cathode via rational surface engineering for both liquid & solid-state sodium ion batteries. *Chem Eng J*. 2021;421:127788. https://doi.org/10.1016/j.cej.2020.127788
91. Zhang F, Liao J, Xu L, Wu W, Wu X. Stabilizing P2-type Ni–Mn oxides as high-voltage cathodes by a doping-integrated coating strategy based on zinc for sodium-ion batteries. *ACS Appl Mater Interfaces*. 2021;13(34):40695-40704. https://doi.org/10.1021/acsami.1c12062
92. Kong W, Wang H, Zhai Y, Sun L, Liu X. Enhancing the rate capability and cycling stability of $Na_{0.67}Mn_{0.7}Fe_{0.2}Co_{0.1}O_2$ through a synergy of Zr^{4+} doping and ZrO_2 coating. *J Phys Chem C*. 2018;122(45):25909-25916. https://doi.org/10.1021/acs.jpcc.8b08742
93. Kaliyappan K, Or T, Deng Y, Hu Y, Bai Z, Chen Z. Constructing safe and durable high-voltage P2 layered cathodes for sodium ion batteries enabled by molecular layer deposition of alucone. *Adv Funct Mater*. 2020;30(17):1910251.
94. Yang L, Sun S, Du K, et al. Prompting structure stability of O3–$NaNi_{0.5}Mn_{0.5}O_2$ via effective surface regulation based on

atomic layer deposition. *Ceram Int*. 2021;47(20):28521-28527. https://doi.org/10.1016/j.ceramint.2021.07.009

95. Kaliyappan K, Liu J, Lushington A, Li R, Sun X. Highly stable $Na_{2/3}(Mn_{0.54}Ni_{0.13}Co_{0.13})O_2$ cathode modified by atomic layer deposition for sodium-ion batteries. *ChemSusChem*. 2015;8(15):2537-2543. https://doi.org/10.1002/cssc.201500155
96. Xiao B, Liu X, Song M, et al. A General strategy for batch development of high-performance and cost-effective sodium layered cathodes. *Nano Energy*. 2021;89:106371. https://doi.org/10.1016/j.nanoen.2021.106371
97. Jiang N, Liu Q, Wang J, et al. Tailoring P2/P3 biphases of layered Na_xMnO_2 by Co substitution for high-performance sodium-ion battery. *Small*. 2021;17(7):2007103.
98. Yan Z, Tang L, Huang Y, et al. A Hydrostable cathode material based on the layered P2@P3 composite that shows redox behavior for copper in high-rate and long-cycling sodium-ion batteries. *Angew Chem Int Ed*. 2019;58(5):1412-1416. https://doi.org/10.1002/anie.201811882
99. Li R, Liu Y, Wang Z, Li J. A P2/O3 biphasic cathode material with highly reversibility synthesized by Sn-substitution for Na-ion batteries. *Electrochim Acta*. 2019;318:14-22.
100. Liang Y, Xu H, Jiang K, Bian J, Guo S, Zhou H. A high-stability biphasic layered cathode for sodium-ion batteries. *Chem Commun*. 2021;57(23):2891-2894.
101. Lamb J, Manthiram A. Synthesis control of layered oxide cathodes for sodium-ion batteries: a necessary step toward practicality. *Chem Mater*. 2020;32(19):8431-8441. https://doi.org/10.1021/acs.chemmater.0c02435
102. Kodera T, Ogihara T. Synthesis and electrochemical properties of $Na_2/3Fe_{1/3}Mn_{2/3}O_2$ cathode materials for sodium ion battery by spray pyrolysis. *J Ceram Soc Jpn*. 2014;122(1426):483-487.
103. Lee SY, Kim JH, Kang YC. Electrochemical properties of P2-type $Na_{2/3}Ni_{1/3}Mn_{2/3}O_2$ plates synthesized by spray pyrolysis process for sodium-ion batteries. *Electrochim Acta*. 2017;225:86-92.
104. Xiao B, Wang Y, Tan S, et al. Vacancy-enabled O3 phase stabilization for manganese-rich layered sodium cathodes. *Angew Chem Int Ed*. 2021;60(15):8258-8267. https://doi.org/10.1002/anie.202016334
105. Lin F, Zhao K, Liu Y. Heterogeneous reaction activities and statistical characteristics of particle cracking in battery electrodes. *ACS Energy Lett*. 2021;6(11):4065-4070. https://doi.org/10.1021/acsenergylett.1c02135
106. Sun Y-K, Chen Z, Noh H-J, et al. Nanostructured high-energy cathode materials for advanced lithium batteries. *Nat Mater*. 2012;11(11):942-947. https://doi.org/10.1038/nmat3435
107. Shin Y, Maeng S, Chung Y, Krumdick GK, Min S. Core–multishell-structured digital-gradient cathode materials with enhanced mechanical and electrochemical durability. *Small*. 2021;17(19):2100040. https://doi.org/10.1002/smll.202100040
108. Chen X, Zhou X, Hu M, et al. Stable layered P3/P2 $Na_{0.66}Co_{0.5}Mn_{0.5}O_2$ cathode materials for sodium-ion batteries. *J Mater Chem A*. 2015;3(41):20708-20714. https://doi.org/10.1039/C5TA05205J
109. Zhou Y-N, Wang P-F, Niu Y-B, et al. A P2/P3 composite layered cathode for high-performance Na-ion full batteries. *Nano Energy*. 2019;55:143-150. https://doi.org/10.1016/j.nanoen.2018.10.072
110. Liu Q, Hu Z, Zou C, Jin H, Wang S, Li L. Structural engineering of electrode materials to boost high-performance sodium-ion batteries. *Cell Rep Phys Sci*. 2021;2(9):100551. https://doi.org/10.1016/j.xcrp.2021.100551
111. Li X, Liu W, Kou H, et al. ALD derived Fe^{3+}-doping toward high performance P2–$Na_{0.75}Ni_{0.2}Co_{0.2}Mn_{0.6}O_2$ cathode material for sodium ion batteries. *Mater. Today Energy*. 2019;14:100353.
112. Quyen NQ, Van Nguyen T, Thang HH, Thao PM, Van Nghia N. Carbon coated $NaLi_{0.2}Mn_{0.8}O_2$ as a superb cathode material for sodium ion batteries. *J Alloys Compd*. 2021;866:158950. https://doi.org/10.1016/j.jallcom.2021.158950
113. Leng M, Bi J, Wang W, et al. Ultrathin MgO coating on fabricated O3–$NaNi_{0.45}Mn_{0.3}Ti_{0.2}Zr_{0.05}O_2$ composite cathode via magnetron sputtering for enhanced kinetic and durable sodium-ion batteries. *J Alloys Compd*. 2021;855:157533. https://doi.org/10.1016/j.jallcom.2020.157533
114. Lamb J, Manthiram A. Surface-modified $Na(Ni_{0.3}Fe_{0.4}Mn_{0.3})O_2$ cathodes with enhanced cycle life and air stability for sodium-ion batteries. *ACS Appl Energy Mater*. 2021;4(10):11735-11742. https://doi.org/10.1021/acsaem.1c02485
115. Jo JH, Choi JU, Konarov A, et al. Sodium-ion batteries: building effective layered cathode materials with long-term cycling by modifying the surface via sodium phosphate. *Adv Funct Mater*. 2018;28(14):1705968. https://doi.org/10.1002/adfm.201705968
116. Tang K, Huang Y, Xie X, et al. The effects of dual modification on structure and performance of P2-type layered oxide cathode for sodium-ion batteries. *Chem Eng J*. 2020;384:123234. https://doi.org/10.1016/j.cej.2019.123234
117. Liu Y, Wang D, Liu J, et al. Surface modification of layer-tunnel hybrid $Na_{0.6}MnO_2$ cathode with open tunnel structure $Na_2Ti_6O_{13}$. *J Alloys Compd*. 2020;849:156441. https://doi.org/10.1016/j.jallcom.2020.156441
118. Zhang Y, Liu L, Jamil S, et al. Al_2O_3 coated $Na_{0.44}MnO_2$ as high-voltage cathode for sodium ion batteries. *Appl Surf Sci*. 2019;494:1156-1165. https://doi.org/10.1016/j.apsusc.2019.07.247
119. Kayyar A, Qian H, Luo J. Surface adsorption and disordering in $LiFePO_4$ based battery cathodes. *Appl Phys Lett*. 2009;95(22):221905.
120. Huang J, Liu H, Zhou N, An K, Meng YS, Luo J. Enhancing the ion transport in $LiMn_{1.5}Ni_{0.5}O_4$ by altering the particle Wulff shape via anisotropic surface segregation. *ACS Appl Mater Interfaces*. 2017;9(42):36745-36754. https://doi.org/10.1021/acsami.7b09903
121. Shin DW, Manthiram A. Surface-segregated, high-voltage spinel $LiMn_{1.5}Ni_{0.42}Ga_{0.08}O_4$ Cathodes with superior high-temperature cyclability for lithium-ion batteries. *Electrochem Commun*. 2011;13(11):1213-1216. https://doi.org/10.1016/j.elecom.2011.08.041
122. Susai FA, Kovacheva D, Chakraborty A, et al. Improving performance of $LiNi_{0.8}Co_{0.1}Mn_{0.1}O_2$ cathode materials for lithium-ion batteries by doping with molybdenum-ions: theoretical and experimental studies. *ACS Appl Energy Mater*. 2019;2(6):4521-4534. https://doi.org/10.1021/acsaem.9b00767
123. George SM. Atomic layer deposition: an overview. *Chem Rev*. 2010;110(1):111-131. https://doi.org/10.1021/cr900056b

124. Zhao Y, Sun X. Molecular layer deposition for energy conversion and storage. *ACS Energy Lett*. 2018;3(4):899-914.
125. Yu F, Du L, Zhang G, Su F, Wang W, Sun S. Electrode engineering by atomic layer deposition for sodium-ion batteries: from traditional to advanced batteries. *Adv Funct Mater*. 2020;30(9):1906890.
126. Kaliyappan K, Liu J, Xiao B, et al. Enhanced Performance of P2-$Na_{0.66}(Mn_{0.54}Co_{0.13}Ni_{0.13})O_2$ cathode for sodium-ion batteries by ultrathin metal oxide coatings via atomic layer deposition. *Adv Funct Mater*. 2017;27(37):1701870. https://doi.org/10.1002/adfm.201701870
127. Puurunen RL. Surface chemistry of atomic layer deposition: a case study for the trimethylaluminum/water process. *J Appl Phys*. 2005;97(12):121301. https://doi.org/10.1063/1.1940727
128. Wang K, Wu Z-G, Melinte G, et al. Preparation of intergrown P/O-type biphasic layered oxides as high-performance cathodes for sodium ion batteries. *J Mater Chem A*. 2021;9:13151-13160.
129. Chen C, Huang W, Li Y, et al. P2/O3 biphasic Fe/Mn-based layered oxide cathode with ultrahigh capacity and great cyclability for sodium ion batteries. *Nano Energy*. 2021;90:106504. https://doi.org/10.1016/j.nanoen.2021.106504
130. Liu Z, Jiang K, Chu S, et al. Integrating P2 into O′3 toward a robust Mn-based layered cathode for sodium-ion batteries. *J Mater Chem A*. 2020;8(45):23820-23826.
131. Eriksson TA, Lee YJ, Hollingsworth J, et al. Influence of substitution on the structure and electrochemistry of layered manganese oxides. *Chem Mater*. 2003;15(23):4456-4463.
132. Dollé M, Patoux S, Doeff MM. Layered Manganese oxide intergrowth electrodes for rechargeable lithium batteries. 1. Substitution with Co or Ni. *Chem Mater*. 2005;17(5):1036-1043.
133. Patoux S, Dollé M, Doeff MM. Layered manganese oxide intergrowth electrodes for rechargeable lithium batteries. 2. Substitution with Al. *Chem Mater*. 2005;17(5):1044-1054.
134. Paulsen J, Dahn J. O_2-type $Li_{2/3}[Ni_{1/3}Mn_{2/3}]O_2$: a new layered cathode material for rechargeable lithium batteries ii. structure, composition, and properties. *J Electrochem Soc*. 2000;147(7):2478.
135. Hu B, Geng F, Zhao C, et al. Deciphering the origin of high electrochemical performance in a novel Ti-substituted P2/O3 biphasic cathode for sodium-ion batteries. *ACS Appl Mater Interfaces*. 2020;12(37):41485-41494. https://doi.org/10.1021/acsami.0c11427
136. Liu G-Q, Li Y, Du Y-L, Wen L. Synthesis and properties of $Na_{0.8}Ni_{0.4}Mn_{0.6}O_2$ oxide used as cathode material for sodium ion batteries. *Rare Met*. 2017;36(12):977-980. https://doi.org/10.1007/s12598-016-0757-9
137. Khan MA, Han D, Lee G, Kim Y-I, Kang Y-M. P2/O3 phase-integrated $Na_{0.7}MnO_2$ cathode materials for sodium-ion rechargeable batteries. *J Alloys Compd*. 2019;771:987-993. https://doi.org/10.1016/j.jallcom.2018.09.033
138. Zhou D, Huang W, Lv X, Zhao F. A novel P2/O3 biphase $Na_{0.67}Fe_{0.425}Mn_{0.425}Mg_{0.15}O_2$ as cathode for high-performance sodium-ion batteries. *J Power Sources*. 2019;421:147-155. https://doi.org/10.1016/j.jpowsour.2019.02.061
139. Lu P, Romero E, Lee S, MacManus-Driscoll JL, Jia Q. Chemical quantification of atomic-scale EDS Maps under thin specimen conditions. *Microsc Microanal*. 2014;20(6):1782-1790. https://doi.org/10.1017/S1431927614013245
140. Liang C, Wang F, Fan W, Zhou W, Tong Y. Transmission electron microscopy analysis of some transition metal compounds for energy storage and conversion. *TrAC Trends Anal Chem*. 2017;90:62-79. https://doi.org/10.1016/j.trac.2017.02.010
141. Muller DA. Structure and bonding at the atomic scale by scanning transmission electron microscopy. *Nat Mater*. 2009;8(4):263-270. https://doi.org/10.1038/nmat2380
142. Kothleitner G, Neish MJ, Lugg NR, et al. Quantitative elemental mapping at atomic resolution using X-ray spectroscopy. *Phys Rev Lett*. 2014;112(8):085501.
143. Devaraj A, Gu M, Colby R, et al. Visualizing nanoscale 3D compositional fluctuation of lithium in advanced lithium-ion battery cathodes. *Nat Commun*. 2015;6(1):1-8.
144. Lu Z, Dahn J. Effects of stacking fault defects on the X-ray diffraction patterns of T_2, O_2, and O_6 structure $Li_{2/3}[Co_xNi_{1/3-x}Mn_{2/3}]O_2$. *Chem Mater*. 2001;13(6):2078-2083.
145. Treacy M, Newsam J, Deem M. A general recursion method for calculating diffracted intensities from crystals containing planar faults. *Proc R Soc Lond Ser Math Phys Sci*. 1991;433(1889):499-520.
146. Casas-Cabanas M, Reynaud M, Rikarte J, Horbach P, Rodriguez-Carvajal J. FAULTS: A program for refinement of structures with extended defects. *J Appl Crystallogr*. 2016;49(6):2259-2269.
147. Thomas G, Bell W, Otte H. Interpretation of electron diffraction patterns from thin platelets. *Phys Status Solidi B*. 1965;12(1):353-366.
148. Yoshida J, Guerin E, Arnault M, et al. New P2—$Na_{0.70}Mn_{0.60}Ni_{0.30}Co_{0.10}O_2$ layered oxide as electrode material for Na-ion batteries. *J Electrochem Soc*. 2014;161(14):A1987-A1991. https://doi.org/10.1149/2.0121414jes
149. Veerasubramani GK, Subramanian Y, Park M-S, et al. Enhanced sodium-ion storage capability of P2/O3 biphase by Li-ion substitution into P2-type $Na_{0.5}Fe_{0.5}Mn_{0.5}O_2$ layered cathode. *Electrochim Acta*. 2019;296:1027-1034.
150. Zhu Y, Xiao Y, Hua W, et al. Manipulating layered P2@ P3 integrated spinel structure evolution for high-performance sodium-ion batteries. *Angew Chem*. 2020;132(24):9385-9390.
151. Xu J, Lee DH, Clément RJ, et al. Identifying the critical role of Li substitution in P2–$Na_x[Li_yNi_zMn_{1-y-z}]O_2$ ($0< x, y, Z< 1$) intercalation cathode materials for high-energy Na-ion batteries. *Chem Mater*. 2014;26(2):1260-1269.
152. Yang L, Li X, Ma X, et al. Design of high-performance cathode materials with single-phase pathway for sodium ion batteries: a study on P2-Na_x $(Li_yMn_{1-y})O_2$ compounds. *J Power Sources*. 2018;381:171-180.
153. Hou D, Xia D, Gabriel E, et al. Spatial and temporal analysis of sodium-ion batteries. *ACS Energy Lett*. 2021;6(11):4023-4054. https://doi.org/10.1021/acsenergylett.1c01868

How to cite this article: Gabriel E, Hou D, Lee E, Xiong H. Multiphase layered transition metal oxide positive electrodes for sodium ion batteries. *Energy Sci Eng*. 2022;10:1672-1705. https://doi.org/10.1002/ese3.1128